Coordination of cell cycle and morphogenesis during organ formation

Jeffrey Matthew, Vishakha Vishwakarma, Thao Phuong Le, Ryan A. Agsunod, and SeYeon Chung*

Department of Biological Sciences, Louisiana State University, Baton Rouge, LA 70803, USA
*Author for correspondence: seyeonchung@lsu.edu

Keywords: *Drosophila*, salivary gland, Huckebein, endoreplication, endocycle, apoptosis, epithelial tube formation

Running title: Hkb regulates endoreplication during *Drosophila* salivary gland morphogenesis

Abstract

Organ formation requires precise regulation of cell cycle and morphogenetic events. Using the *Drosophila* embryonic salivary gland (SG) as a model, we uncover the role of the SP1/KLF transcription factor Huckebein (Hkb) in coordinating cell cycle regulation and morphogenesis. The *hkb* mutant SG exhibits defects in invagination positioning and organ size due to abnormal death of SG cells. Normal SG development involves distal-to-proximal progression of endoreplication (endocycle), whereas *hkb* mutant SG cells undergo abnormal cell division, leading to cell death. Hkb represses the expression of key cell cycle and pro-apoptotic genes in the SG. Knockdown of *cyclin E* or *cyclin-dependent kinase 1,* or overexpression of *fizzy-related* rescues most of the morphogenetic defects observed in the *hkb* mutant SG. These results indicate that Hkb plays a critical role in controlling endoreplication by regulating the transcription of key cell cycle effectors to ensure proper organ formation.

Introduction

The formation of tubular organs, such as the lungs and kidneys, begins with the folding of flat epithelial tissues into functional three-dimensional (3D) tubular structures. In humans, errors in tube formation can result in congenital defects such as spina bifida and lung hypoplasia (Wilde et al., 2014). Studies in both vertebrates and invertebrates have revealed key morphogenetic mechanisms underlying epithelial tube formation during development (Andrew and Ewald, 2010, Chung et al., 2014, Herriges and Morrisey, 2014, Girdler and Röper, 2014, Nikolopoulou et al., 2017, Spina and Cowin, 2021, Pradhan et al., 2023). While proper cell shape changes and cell rearrangement are critical, precise regulation of cell division and cell death is also essential for tissue morphogenesis (Huh et al., 2004, Mao et al., 2013, LeGoff and Lecuit, 2015, Godard and Heisenberg, 2019). Notably, the interplay between cell division and cell death provides a homeostatic control system necessary for proper organ formation. Perturbations at any stage of the cell cycle can have detrimental effects on cell viability, leading to cell death, and activation of apoptosis can trigger compensatory proliferation in surrounding cells (Ryoo et al., 2004). In addition to their role in establishing and maintaining the correct number of cells in tissues and organs, cell division and cell death generate biophysical forces through actomyosin reorganization that help shape the final tissue morphology. For example, during *Drosophila* tracheal invagination, mitotic cell rounding drives the internalization of the tracheal primordium (Kondo and Hayashi, 2013). During dorsal closure and leg folding in *Drosophila* (Toyama et al., 2008, Monier et al., 2015) and neural closure in mammals (Massa et al., 2009, Yamaguchi et al., 2011), apoptotic cells generate forces at both local and tissue scales that affect tissue remodeling. Therefore, to fully understand the mechanisms of organ formation, it is critical to know how the cell cycle, cell death, and morphogenesis are coordinated during epithelial tube formation.

The *Drosophila* embryonic salivary gland (SG) is a premier model for studying the mechanisms of tube formation from a flat epithelial sheet (Chung et al., 2014, Sidor and Röper, 2016). The *Drosophila* embryo contains two SGs, each consisting of 140-150 cells, which initially reside on the embryo surface and invaginate to form single-layered, elongated tubes (Fig. 1A). Once SG cells are specified, they do not divide or die. Cell death is actively inhibited during SG morphogenesis. The SG-upregulated transcription factors Fork head (Fkh), Senseless, and Sage inhibit apoptosis by downregulating proapoptotic genes, such as *head involution defective* (*hid*)

70 and *reaper* (*rpr*) (Myat and Andrew, 2000a, Chandrasekaran and Beckendorf, 2003, Fox et al.,
71 2013). Instead of cell division, SG cells undergo endoreplication (endocycle), a variant of the
72 cell cycle that involves DNA replication without subsequent cell division forming polyploid
73 cells, upon invagination at stage 11 (Follette et al., 1998). SG cells that have completed one
74 round of endoreplication arrest the cell cycle in G2 until the larval stage (Smith and Orr-Weaver,
75 1991, Chandrasekaran and Beckendorf, 2005). Endoreplication, which is more common in
76 invertebrates and plants, was thought to be a rare cell cycle variation in mammals. However,
77 recent studies have revealed endoreplication in various mammalian tissues, including humans,
78 and endoreplication is emerging as a potential developmental timer (Gandarillas et al., 2018).
79 Like the conventional cell cycle, endoreplication is regulated by key cell cycle genes such as
80 cyclins and cyclin-dependent kinases (CDKs). In *Drosophila* embryogenesis, re-entry into S
81 phase during endoreplication is regulated by the cyclin E-Cdk2 complex through the E2F
82 proteins (Duronio et al., 1995, Follette et al., 1998). Because SG morphogenesis occurs in the
83 absence of cell division and cell death, studies of SG morphogenesis have primarily focused on
84 the mechanisms underlying cell shape changes, cell intercalation, and collective cell migration
85 (Pirraglia et al., 2010, Xu et al., 2011, Röper, 2012, Ismat et al., 2013, Booth et al., 2014, Chung
86 et al., 2014, Chung et al., 2017, Sanchez-Corrales et al., 2018, Sanchez-Corrales et al., 2021, Le
87 and Chung, 2021, Vishwakarma et al., 2022). Little is known about the potential impact of
88 regulating endoreplication and cell death during SG morphogenesis.

89 Invagination is the first step in SG morphogenesis that is critical for organ architecture, and
90 studies in recent years have revealed key underlying molecular and cellular mechanisms (Chung
91 et al., 2017, Sanchez-Corrales et al., 2018, Sidor et al., 2020, Sanchez-Corrales et al., 2021, Le
92 and Chung, 2021, Vishwakarma et al., 2022). SG invagination occurs in a stereotypical manner,
93 with two predominant cell behaviors occurring in distinct spatial domains within the placode
94 relative to the invagination pit forming in the dorsal/posterior region: clustered apical
95 constriction near the pit (Fig. 1A) and cell intercalation far from the pit. Two early-expressed
96 SG-upregulated transcription factors, Fkh and Huckebein (Hkb), play critical roles in SG
97 invagination. Fkh, a winged-helix transcription factor that regulates more than two-thirds of the
98 known SG genes, is essential for SG invagination; SG cells fail to invaginate in *fkh* mutants in
99 which apoptosis is inhibited (Myat and Andrew, 2000a, Maruyama et al., 2011). Hkb, an
100 SP1/KLF transcription factor, is crucial for invagination positioning; SG cells invaginate in the

central region of the placode in *hkb* mutants (Myat and Andrew, 2000b). A recent study proposed that the early patterning of Fkh and Hkb and their downstream effectors ensures positionally fixed cell behaviors with respect to invagination position (Sanchez-Corrales et al., 2021). For example, a key downstream target of Fkh, Folded gastrulation (Fog), signals through its G protein-coupled receptor to activate Rho kinase and myosin to regulate apical constriction in the dorsal/posterior region of the SG placode (Chung et al., 2017, Vishwakarma et al., 2022). Despite the intriguing phenotype of *hkb* mutants, the mechanism of how Hkb regulates SG invagination positioning remains largely unknown. Only two potential downstream targets of Hkb involved in SG formation have been identified: *crumbs* (*crb*), encoding a key apical membrane protein, and *klarsicht* (*klar*), encoding a Nesprin family protein that mediates dynein-dependent organelle trafficking (Myat and Andrew, 2002). To fully understand the mechanism of how Hkb regulates invagination position, it is critical to reveal the precise cellular mechanisms underlying the centered invagination phenotype and identify Hkb downstream targets regulating the process.

In this study, we reveal the distal-to-proximal progression of endoreplication during SG morphogenesis and show that Hkb plays a critical role in this process. Loss of *hkb* results in abnormal cell division in the SG leading to cell death. Subsequently, abnormal cell death leads to malposition of the SG invagination and formation of a smaller organ. Using modENCODE Hkb ChIP-Seq targets and genetic interaction analyses, we show that Hkb represses the transcription of key cell cycle genes in the SG to control cell cycle progression and ensure cell survival and proper SG morphogenesis.

Materials and Methods

Fly stocks and genetics

The fly stocks used in this study are listed in Table S1. All the crosses were performed at 25°C.

Generation of *hkb* mutant alleles

hkb mutant alleles were generated using CRISPR/Cas9. Using flyCRISPR Target Finder (http://targetfinder.flycrispr.neuro.brown.edu/), we identified two gRNAs, one in the first exon of the *hkb* transcript near the 5' end of the gene (gRNA3) and the other in the second zinc finger domain (gRNA1). Both gRNAs exhibited maximum stringency, with zero predicted off-target effects. The sense and antisense oligos for each gRNA sequence were annealed and cloned into the pU6-BsaI-gRNA vector (a kind gift from Jean-Paul Vincent; (Baena-Lopez et al., 2013)) via the BsaI restriction site. The constructs were confirmed by Sanger sequencing before injection. The following sense and antisense oligonucleotides were used for creating null (gRNA3) and hypomorphic (gRNA1) alleles (PAM sequences underlined and linkers in small characters).

gRNA1 sequence: 5'-ACGCGTCAGTTCCTCATTGCGGG-3'
sense oligo, 5'-tccACGCGTCAGTTCCTCATTGC-3'
antisense oligo, 5'-aaacGCAATGAGGAACTGACGCGT-3'

gRNA3 sequence: 5'-AAAGTCGCGAGTAGGTTTGCGGG-3'
sense oligo, 5'-tccAAAGTCGCGAGTAGGTTTGC-3'
antisense oligo, 5'-aaacGCAAACCTACTCGCGACTTT-3'

The pU6-gRNA1/3 constructs (500 ng/µl per gRNA) were sent to GenetiVision for injections. GenetiVision performed injection into nos-Cas9 embryos. Individual G0 adults were crossed to w; TM3, Sb/TM6B, Tb flies. Five offspring (F1) for each cross were independently crossed to w; TM3, Sb/TM6B, Tb to generate independent stocks. The DNA fragment encompassing the gRNA sites was PCR amplified using a single adult fly of each stock, and indels at the corresponding gRNA site were confirmed by Sanger sequencing. The following primers were used for both PCR and sequencing.

153 Hkb_FWD, 5’-AGATTGGGTTTGGTGAGTGC-3’
154 Hkb_REV, 5’-TCGCACATCCTCAGACAGAC-3’

155 The predicted protein sequences and details of indels for each allele were described in Sup. Fig.
156 S1.

157

158 **Generation of Hkb-mCherry fusion protein lines**
159 To create the functional Hkb-mCh fusion protein line, mCherry was inserted into six amino acids
160 upstream from the C-terminal end of the Hkb protein in frame with the Hkb protein using the
161 homology-directed repair of the CRISPR/Cas9 technique. The gRNA near the C-terminal end of
162 the protein was chosen (Hkb_C_gRNA3, 5’-CCCATGTACTCATACCTTTATGG-3’) using the
163 flyCRISPR Target Finder (http://targetfinder.flycrispr.neuro.brown.edu/). Genomic DNA regions
164 that flank the gRNA locus were amplified using the WT genomic DNA for the left and right
165 homology arms (HAL (1066 bp) and HAR (1408 bp)). DNA fragments for the open reading
166 frame of the mCherry protein and the backbone plasmid were amplified using the pENTR R4-
167 mCherry-R3 plasmid (Addgene #32311) as a template. The donor DNA construct containing
168 both homology arms (pENTR-HAL-mCherry-HAR; 5853 bp) was created using the NEBuilder
169 HiFi DNA Assembly Master Mix (NEB #E2621). The following primers were used for
170 amplifying each DNA fragment.
171

172 mCh_FWD, 5’-CCATCTTCGTGCCCATGTACATGGTGAGCAAGGGCGAG-3’
173 mCh_REV, 5’-CTTGTACAGCTCGTCCATGC-3’
174 Backbone_FWD, 5’-CTATGCCGTCTCCATTCGATACAACTTTGTATAATAAAGTTGAAC-
175 3’
176 Backbone_REV, 5’-GTTGGCCAACTTTGTATAG-3’
177 HAL_FWD, 5’-TCTATACAAAGTTGGCCAACAGATCTCGCAGCACACAC-3’
178 HAL_REV, 5’-GTACATGGGCACGAAGATG-3’
179 HAR_FWD, 5’-GCATGGACGAGCTGTACAAGTCATACCTTTATGGCTACTGAG-3’
180 HAR_REV, 5’-ATCGAATGGAGACGGCATAG-3’
181

182 The same strategy was used to create the Hkb^{mut}-mCh knock-in line. The mCh tag was inserted
183 into the N-terminal region of Hkb, using gRNA3, the same gRNA used to create null mutant
184 alleles. A stop codon was added to the C-terminal end of the mCh tag. Genomic DNA regions
185 that flank the gRNA locus were amplified using the WT genomic DNA for the left and right
186 homology arms (HAL (1130 bp) and HAR (1153 bp)). The following primers were used for
187 amplifying each DNA fragment.
188
189 mCh_FWD, 5'- CCCGCAAATGGTGAGCAAGGGC -3'
190 mCh_REV, 5'- GCGAGTAGGTCTACTTGTACAGCT-3'
191 Backbone_FWD, 5'-
192 AAATATTGAGATACAACTTTGTATAATAAAGTTGAACGAGAAACGTAAAA -3'
193 Backbone_REV, 5'- TGGCTGCAGTTGGCCAACTTTGTATAGAAAAGTTGAAC -3'
194 HAL_FWD, 5'- GGCCAACTGCAGCCAGAATCGCG -3'
195 HAL_REV, 5'- CTCACCATTTGCGGGGGATG -3'
196 HAR_FWD, 5'- TACAAGTAGACCTACTCGCGACTTTTCC-3'
197 HAR_REV, 5'-
198 TATACAAAGTTGTATCTCAATATTTGCATATATCGTCGAGGTCCAAAGA -3'
199
200 The pENTR-HAL-mCherry-HAR constructs (500 ng/µl per gRNA) were sent to GenetiVision
201 for injections. GenetiVision performed injection into nos-Cas9 embryos. Individual G0 adults
202 were crossed to w; TM3, Sb/TM6B, Tb flies. Five offspring (F1) from each of the surviving
203 crosses were independently crossed to w; TM3, Sb/TM6B, Tb to generate independent stocks.
204 Fluorescent signals for mCherry in Hkb^{WT}-mCh and Hkb^{mut}-mCh transgenic lines were confirmed
205 by immunostaining using the antibody against mCherry.
206

207 **Immunostaining and imaging**

208 *Drosophila* embryos were collected on grape juice agar plates at 25°C. Embryos were
209 dechorionated by incubating in 50% bleach for 3 minutes. For most samples, embryos were fixed
210 in formaldehyde-saturated heptane for 40 minutes and devitellinized using 80% ethanol.
211 Following this, the embryos were stained with primary and secondary antibodies in PBSTB (1X

212 PBS, 0.2% bovine serum albumin, and 0.1% Triton X-100). For phalloidin and sqh-GFP signals,
213 embryos were hand-devitellinized and stained with primary and secondary antibodies in PBTr
214 (1X PBS and 0.1% Triton X-100). The antibodies used in this study and their respective dilutions
215 are listed in Table S2. After staining, embryos were mounted in Aqua-Poly/Mount (Polysciences,
216 Inc.) and imaged with Leica SP8 confocal microscope using 63x, NA 1.4 and 40x, NA 1.3
217 objectives. For horseradish peroxidase (HRP) staining, the VECTASTAIN® ABC-HRP Kit,
218 Peroxidase (PK-4000; Vector Laboratories) was used with biotin-conjugated secondary
219 antibodies. Whole embryo HRP images were acquired with a Leica DM2500 microscope using a
220 20×, 0.8 NA objective.

221

222 **Cell segmentation, apical area quantification, and scatter plots**

223 SGs in early (pre-invagination; invagination depth, 0 µm) and late (during invagination;
224 invagination depth, 5-10 µm) stage 11 of embryos were used. Confocal images of the SG were
225 obtained from embryos immunostained for the Ecad (adherens junctions) and CrebA (SG cell
226 nuclei) and used for cell segmentation. A maximum intensity projection was generated using the
227 LasX program from three apical z-sections of confocal images of SG cells encompassing the
228 adherens junction. Using the maximum intensity projection, cells were segmented using Ecad
229 signals as a marker for each cell boundary using Imaris software (Andor). The apical area was
230 calculated using Imaris and individual cells were color-coded based on the size of their apical
231 areas. The frequency distribution of the apical area of the cells was analyzed using GraphPad
232 Prism with the data exported from Imaris. Since the output data from Imaris for the apical area
233 quantification is a sum of the area of both sides of the cell layer, we further divided the values by
234 2 to obtain the apical area of SG cells.

235 Scatter plots were generated using the X and Y coordinates for each SG cell, which were
236 determined with respect to the A/P and D/V axes of the tissue using Imaris. The cell at the center
237 of the SG placode was used as the origin point (X=0, Y=0).

238

239 **Quantification of SG cell numbers**

240 Confocal microscopy stacks for SGs with nuclear markers (CrebA or Sage) were used for early
241 stage 11 (pre-invagination) and stage 15+ embryos. Three dimensional (3D)-reconstructed
242 images were generated using Imaris. The number of nuclei for each 3D-reconstructed SG was
243 counted using cell ID numbers.

244

245 **Quantification of SG lumen length and apical area of individual SG cells at stage 15**

246 Confocal images immunolabeled with markers for Ecad and CrebA for stage 15 SGs were used.
247 8-12 z-section images of the SG were merged to obtain a maximum projection image clearly
248 showing half of the SG lumen and its apical surface. Segmentation of SG cells and quantification
249 of apical areas of individual cells were performed using Imaris as described for segmentation of
250 SG cells at stage 11.

251 For the lumen length quantification, maximum intensity projection images were imported into
252 the ImageJ software (Fiji). The length of the SG lumen was measured along the line following
253 the midpoint of the secretory portion of the tube.

254

255 **Quantification of SG phenotypes at embryonic stages 12 and 15+**

256 After performing HRP staining with CrebA, the SGs were manually categorized based on their
257 phenotypes. At stage 12, WT SGs turn and migrate towards the posterior of the embryo after
258 reaching the visceral mesoderm. SGs showing such normal behavior were categorized as
259 "normal", while those SGs that reached the visceral mesoderm and migrated slightly were
260 categorized as "turned but short", and those SGs that reached the visceral mesoderm but did not
261 migrate posteriorly were categorized as "not turned".

262 For stage 15+ embryos, SGs that were comparable in shape, size, and position to WT SGs were
263 categorized as "normal"; embryos in which both SGs showed rounded/ball-like morphology
264 were categorized as "very short/rounded"; SGs that were slightly elongated but not as long as
265 WT SGs and localized in the anterior/center were categorized as "short, both ant./center".
266 Embryos in which SGs were shorter than WT and one of the SGs was localized in the

267 anterior/center were categorized as “short, one ant./center”; embryos in which SGs were in the
268 normal position but were short in length were categorized as “short, normal position”.

269

270 **Analysis of modENCODE Hkb ChIP-Seq targets**

271 The dataset was downloaded from the ENCODE Portal (https://www.encodeproject.org/). Total
272 1268 ChIP-Seq targets were analyzed using Database for Annotation, Visualization and
273 Integrated Discovery (DAVID; Dennis et al., 2003).

274

275 **Fluorescence in situ hybridization**

276 Dechorionated *Drosophila* embryos were fixed in paraformaldehyde-heptane solution for 30
277 min, followed by devitellinization using methanol. Freshly fixed embryos were then labeled with
278 digoxigenin (DIG)-labeled antisense probes following the standard procedure described in Knirr
279 et al. (1999). After rehydration and post-fixation in 10% formaldehyde, embryos were pre-
280 hybridized for 1 hour at 55°C. mRNA probes were added to the embryos which were then
281 incubated for 16 hours at 55°C. DIG present on the synthesized mRNA probes was subsequently
282 labeled with anti-DIG primary antibody (Enzo; ENZ-ABS302-0001; 1:1,000) and biotin-
283 conjugated secondary antibody (Invitrogen; 1:500). To detect fluorescent signals, embryos were
284 incubated with AB solution (PK-6100, Vectastain Elite ABC kit) followed by the tyramide signal
285 amplification reaction (Cy3 fluorescent dye in amplification diluent; 1:50) (Perkin Elmer Life
286 Sciences, NEL753001kt). To mark the SG and the apical membrane, the embryos were
287 immunolabeled with antibodies for CrebA (SG nuclei) and Crb (apical membrane).

288 Primer sequences used for mRNA probe synthesis in this study are listed below.

Gene name	Primer sequence	Probe size
Cyclin A (*CycA*)	Forward: 5’-TAAACCACGAACCGCTGAAC-3’	443 bp

	Reverse: 5’-CATGGTGCGCTCTTTCCTAC-3’	
Cyclin D (*CycD*)	Forward: 5’-CCCAGAACAATGCCGTAGTG-3’ Reverse: 5’-CCATTCGGCGACAATTTTGC-3’	404 bp
Cyclin E (*CycE*)	Forward: 5’-TGGACTGGTTGATCGAGGTC-3’ Reverse: 5’-TCAAAGCCAGAGAATTGCGG-3’	424 bp
E2f1	Forward: 5’-CAGTCCGCAAAAATGTGAAA-3’ Reverse: 5’-TATCACACGCAACCACAACA-3’	500 bp
forkhead (*fkh*)	Forward: 5’-TCGATCCGCCTACACAATGA-3’ Reverse: 5’-ATGGCCATGGTGATCAGTGA-3’	483 bp
fizzy-related (*fzr*)	Forward: 5’-ACCCCACAGCAGCAATAGAT-3’ Reverse: 5’-TTCGGGGGTATGAGTGTTTC-3’	417 bp
head involution defect (*hid*)	Forward: 5’-CCCGCAAATCTTCCAGTATC-3’ Reverse: 5’-GTGTAGCCCGCGTAGTAGGT-3’	339 bp
reaper (*rpr*)	Forward: 5’-CGAAAGAAAAGTGTGTGCGC-3’ Reverse: 5’-GTTGTGGCTCTGTGTCCTTG-3’	483 bp

289

290

291

292

Results

Creation of the molecularly defined *hkb* mutant alleles and fluorescent knock-in lines

To fully characterize the role of Hkb during SG morphogenesis, we generated two null (hkb^{351}, hkb^{391}) and two hypomorphic alleles (hkb^{121}, hkb^{131}) using CRISPR/Cas9 (Fig. 1B; Details of indels and expected protein sequences were described in Sup. Fig. S1). All alleles were embryonic lethal in homozygous embryos and transheterozygotes with a deficiency line deleting the *hkb* locus, suggesting that all three zinc-finger (ZnF) domains are required for embryonic development and survival. Immunostaining with CrebA, a SG nuclear marker, and E-Cadherin (Ecad), an adherens junction marker, showed that wild-type (WT) embryos exhibited SG invagination in the dorsal-posterior region of the placode (Fig. 1C). However, the new *hkb* null alleles exhibited a broad, central SG invagination phenotype (Fig. 1E), similar to previous studies with undefined strong hypomorphic EMS alleles, hkb^{2} and hkb^{A321R1} (Weigel et al., 1990, Gaul and Weigel, 1990, Myat and Andrew, 2002, Sanchez-Corrales et al., 2021). hkb^{121} and hkb^{131} also exhibited the centered invagination phenotype, albeit with lower penetrance (Fig. 1D; 50%, N=20 SGs for hkb^{121}; data not shown for hkb^{131}), indicating that all three ZnF domains are required for the positioning of the SG invagination.

To investigate the effect of *hkb* loss on SG cell behavior during invagination, we analyzed the distribution of SG cells undergoing apical constriction in WT and *hkb* mutants using cell segmentation analysis (Fig. 1H-K'; Sup. Fig. S2A-F'). Before invagination, WT SG cells with small apical areas clustered in the dorsal-posterior region of the placode, whereas *hkb* mutants exhibited a scattered distribution (Sup. Fig. S2D-F'). As invagination progressed, more cells with small apical areas were observed near the invagination pit in WT, whereas these cells were distributed around the wide central pit in *hkb* mutant SGs (Fig. 1H-J'). This is consistent with a previous study using hkb^{2} (Sanchez-Corrales et al., 2021), although we observed that only about 30% of the hkb^{2} embryos showed the central SG invagination phenotype (N=11). The frequency distribution of cells based on their apical areas showed a significantly lower percentage of SG cells with smaller apical areas in *hkb* mutants compared to WT (Fig. 1K, K'; Sup. Fig. S2G, G'), indicating a defect in apical constriction.

321 Using CrebA signals, we analyzed SG morphology in late-stage WT and *hkb* mutant embryos. At
322 stage 12, while the WT SGs turned and migrated toward the posterior of the embryo upon
323 reaching the visceral mesoderm, SGs in *hkb* mutant embryos migrated only slightly posteriorly
324 (Fig. 1L-N; Sup. Fig. S3A-E). Consistent with the role of Hkb in endoderm specification
325 (Brönner et al., 1994), *hkb* mutant embryos showed defects in gut morphology, as well as defects
326 in head development and occasional defects in germ band retraction (Fig. 1L'-N'; Sup. Fig.
327 S3A'-E'), making it difficult to determine their correct stage after stage 14. Stage 15+ embryos
328 in *hkb* mutants formed small SGs compared to stage 15 WT embryos (Fig. 1L'-N'; Sup. Fig.
329 S3A'-E'), as in a previous study (Myat and Andrew, 2000b). We observed a range of SG lengths.
330 More than 40% of stage 15+ *hkb* null (hkb^{351} and hkb^{391}) embryos exhibited very short and ball-
331 like SGs (Fig. 1N', O'; Sup. Fig. S3C', F'). In contrast, the majority of *hkb* hypomorphic
332 mutants (hkb^{121} and hkb^{131}) and other non-molecularly defined *hkb* mutants (hkb^{A321R1} and hkb^{2})
333 had intermediate SG tube lengths (Fig. 1M', O'; Sup. Fig. S3B', D'-E', F'), further suggesting
334 that hkb^{A321R1} and hkb^{2} have a residual function of *hkb*.

335 In all *hkb* mutant lines, one or both SGs frequently mislocalized anteriorly, toward the head
336 center region (Fig. 1M', N'; Sup. Fig. S3C'-E'). Using the salivary duct marker Dead Ringer
337 (Dri; (Gregory et al., 1996)) and Ecad, we found that the mispositioning of the SG was due to the
338 malformation of the duct, likely resulting from a combination of reduced cell number, aberrant
339 apical domain size, and defective cell intercalation of duct cells (Sup. Fig. S4A-H). These data
340 suggest that Hkb has an additional role in salivary duct morphogenesis.

341 We also generated two mCherry-tagged transgenic lines, Hkb^{WT}-mCh (a functional fusion
342 protein line) and Hkb^{mut}-mCh (a mutant knock-in line) using CRISPR-mediated homology-
343 directed repair (Fig. 1B). The Hkb^{WT}-mCh line exhibited nuclear mCh signals in several tissues
344 known to express Hkb, including the anterior and posterior termini of the early embryo, SGs, and
345 a subset of neuroblasts (Fig. 1F, F'; Sup. Fig. S5C-J''). In the SG, strong Hkb^{WT}-mCh signals
346 were detected at stages 10 and 11, with higher levels in the posterior region of the placode at
347 stage 10 (Sup. Fig. S5C-D''), consistent with a previous study (Sanchez-Corrales et al., 2021).
348 Weak Hkb^{WT}-mCh signals were present at stages 12 and 13 and not detected thereafter (Sup. Fig.
349 S5H-I''), consistent with the transient expression of *hkb* transcripts in the SG (Myat and Andrew,
350 2002). Unlike the nuclear Hkb^{WT}-mCh signals, Hkb^{mut}-mCh signals were distributed throughout

351 the cell (Fig. 1G, G'; Sup. Fig. S5M-T''). In homozygous Hkb^{mut}-mCh and heterozygous
352 Hkb^{mut}-mCh/+ embryos, mCh signals persisted throughout the SG cell until stage 16, likely due
353 to the long half-life of the mCh protein (Sup. Fig. S5J-J'' and T-T''). Homozygous Hkb^{mut}-mCh
354 embryos exhibited the same range of phenotypes as *hkb* null mutants, confirming that the mCh
355 insertion disrupts Hkb function (Fig. 1G; Sup. Fig. S5O-P'').

356 Together, we have generated molecularly defined null and hypomorphic alleles of *hkb* and
357 fluorescently tagged knock-in transgenic lines. Since the two null and two hypomorphic alleles
358 behaved similarly, we used *hkb*^{351} and *hkb*^{121} for further analyses.

359

360 **Hkb is required for SG cell survival**

361 To determine the cellular mechanisms underlying the small SG phenotype in *hkb* mutant
362 embryos, we measured the SG lumen length and counted SG cells using Ecad and CrebA signals,
363 respectively. Compared to WT, *hkb* null mutants and transheterozygous *hkb* null over a
364 deficiency showed a significantly shorter SG lumen length (Fig. 2A-D, G), and *hkb* hypomorphic
365 embryos showed a milder effect. Surprisingly, *hkb* null mutants also showed fewer SG cells
366 compared to WT, with a moderate reduction at stage 11 and a significant reduction at stage 15
367 (stage 15+ for *hkb* mutants). The effect was milder in hypomorphic embryos, indicating a
368 correlation between the SG lumen length and the number of cells (Fig. 2G', G'').

369 To test whether *hkb* mutant SG cells undergo apoptosis, we labeled WT, *hkb* mutant, and Hkb^{WT}-
370 mCh and Hkb^{mut}-mCh embryos with an antibody against *Drosophila* cleaved death caspase-1
371 (DCP-1; (Sarkissian et al., 2014)). WT and Hkb^{WT}-mCh SG cells showed no DCP-1 signals (Fig.
372 2H, N), except for a single cell at the anterior boundary of the SG placode in some stage 11
373 embryos (data not shown). In contrast, SGs in *hkb* mutants and Hkb^{mut}-mCh embryos displayed
374 significant DCP-1 signals at stages 11 and 12 (Fig. 2I-K, O, P; Sup. Fig. S7A-B'). DAPI staining
375 revealed condensed and fragmented nuclei in some SG cells in *hkb* mutants (Fig. 2Q, Q'), a
376 hallmark of pyknosis (Zamzami and Kroemer, 1999). At stages 13 and 14, several fragmented
377 cells positive for DCP-1 and mCh, and negative for CrebA, were found near the SG in Hkb^{mut}-
378 mCh embryos (Sup. Fig. S7C, C'). Similar DCP-1-positive cells were found near the SG in *hkb*

null mutants, fewer in *hkb* hypomorphs, and rarely in WT embryos (Sup. Fig. S7C-D'). These cells, lacking CrebA signals but exhibiting nuclear fragmentation and condensation, are likely late-stage apoptotic SG cells. Increased DCP-1 signals were also detected in several other parts of the Hkb^{mut}-mCh embryos near mCh-expressing regions compared to Hkb^{WT}-mCh embryos (Fig. S7G-I''), suggesting a role for Hkb in cell survival in multiple cell types.

Expression of Hkb in the SG using the *fkh-Gal4* driver (Henderson and Andrew, 2000) reduced the number of DCP-1-positive SG cells in *hkb* mutants (Fig. 2L, P). This partially rescued the short SG phenotype of *hkb* mutants, resulting in a range of SG lengths, from elongated SGs resembling WT to very short SGs resembling *hkb* mutants, and intermediate-length SGs (Fig, 2F; Sup. Fig. S6A-D, I, J). Elongated SGs restored lumen length and SG cell number to WT levels (Fig. 2E, G''). Additionally, blocking apoptosis in the *hkb* mutant SG by overexpressing the baculoviral protein p35, a caspase inhibitor of apoptosis, reduced the number of DCP-1-positive cells (Fig. 2M, P) and partially rescued the shortened SG phenotype, with restored SG cell number (Fig. 2G''; Sup. Fig. S6E-J). These data suggest that the small SG size in *hkb* mutants is primarily caused by apoptosis of SG cells.

Hkb is required for apical domain elongation

A previous study showed that *hkb* regulates apical domain elongation by regulating the key apical protein Crb and the endocytic pathway regulator Klar (Myat and Andrew, 2002). Although our data showed that the reduced number of SG cells is the main reason for the small gland size in *hkb* mutants, defects in apical domain elongation may also contribute to this phenotype. Measuring the apical area of individual SG cells in stage 15 embryos revealed that *hkb* mutant SG cells have smaller apical domain sizes than WT (Sup. Fig. S8A-E). Immunostaining with Rab11, a recycling endosome marker, revealed that while WT SGs showed Rab11 signals near the apical domain, *hkb* mutant SGs displayed basally mislocalized Rab11 signals (Sup. Fig. S8F, G). These data suggest that impaired apical trafficking and defective apical membrane elongation also contribute to the small gland phenotype in *hkb* mutants.

407 **Aberrant cell death causes centered SG invagination in *hkb* mutants**

408 Next, we tested invagination positioning. SG-specific expression of Hkb corrected the centered
409 invagination defect in *hkb* mutants (Fig. 3A-C), indicating a tissue-autonomous role of Hkb in
410 SG invagination positioning. Interestingly, blocking apoptosis in the SG also rescued the
411 centered invagination phenotype in *hkb* mutants (Fig. 3D). Cell segmentation analysis revealed
412 that cells with small apical areas were mainly distributed in the dorsal/posterior quadrant of the
413 SG placode in these embryos (Fig. 3E-F'), as in WT (Fig. 1H'). Since apoptotic cells undergo
414 apical constriction before being eliminated from the epithelial sheet (Toyama et al., 2008,
415 Slattum et al., 2009, Marinari et al., 2012), we hypothesized that some SG cells with small apical
416 areas in *hkb* mutants are apoptotic. In support of this, we observed DCP-1-positive cells with
417 reduced apical areas in *hkb* mutant SGs at stage 11 (Fig. 3E). Among the SG cells of lower 30%
418 of apical areas, more than 40% were DCP-1-positive (N=29/72 cells in 5 SGs). We did not detect
419 a significant spatial bias in the distribution of DCP-1-positive cells among the four quadrants of
420 the SG placode in *hkb* null mutants, although slightly more DCP-1-positive cells were observed
421 in the posterior region in hypomorphs and transheterozygotes of null over deficiency (Fig. 3H, I).
422 When we analyzed the SG placode in three domains (inner, outer, and mid), we found that most
423 DCP-1-positive cells were in the mid domain, especially in the null and transheterozygous
424 conditions (Fig. 3I'). This suggests a correlation between the distribution of dying cells in the
425 mid domain and the widened central invagination pit observed in *hkb* mutants.

426 During apoptosis, the cytoskeleton actively participates in the morphological changes of dying
427 cells. Apoptotic cells also exert a transient pulling force on the apical surface, generating the
428 apicobasal force and increasing tissue tension (Monier et al., 2015). Therefore, we analyzed
429 filamentous actin (F-actin) and myosin using phalloidin and sqh-GFP, a functional tagged
430 version of the myosin regulatory light chain (Royou et al., 2004), respectively, in WT and *hkb*
431 mutant SGs. Compared to WT, we often observed an aberrant accumulation of F-actin and
432 myosin signals along multiple junctions within the SG placode in *hkb* mutants (Fig. 3J-N). In
433 addition, there was placode-wide disruption of myosin, including the misshapen supracellular
434 myosin cable that maintains SG tissue integrity (Fig. 3K). Apical junctions with increased
435 myosin or F-actin levels often coincided with DCP-1-positive cells (Fig. 3L, M-N). Increased F-

436 actin expression was also seen at the apical-lateral membrane of DCP-1 positive cells (Fig. 3N),
437 suggesting a potential pulling force along the apicobasal axis by apoptotic cells.

438

439 **Hkb is required for the proper cell cycle status in the SG**

440 To further test the impact of *hkb* loss in cytoskeletal organization, we analyzed microtubules,
441 which play a crucial role in forming and maintaining the actomyosin network during tissue
442 invagination (Booth et al., 2014, Ko et al., 2019, Le and Chung, 2021). Interestingly,
443 immunostaining with an antibody against tyrosinated α-tubulin (Tyr-tub), which labels dynamic,
444 short-lived microtubules (Westermann and Weber, 2003) revealed that, in contrast to the strong
445 Tyr-tub signals observed at the apices of WT SG cells (Fig. 4A, A'; (Booth et al., 2014, Le and
446 Chung, 2021)), some SG cells in *hkb* mutants lacked apical Tyr-tub signals (Fig. 4B, B'). These
447 cells had large, rounded morphology and mislocalized nuclei near the apical surface (Fig. 4C, D),
448 indicating cell division. Staining with an antibody against phosphorylated histone H3 (PH3), a
449 marker of mitotic chromatin modification (Gurley et al., 1978), revealed strong PH3 signals in
450 *hkb* mutant SG cells (Fig. 4E-H, M), indicating that these cells are actively dividing. Co-staining
451 with Tyr-tub and PH3 revealed that mitotic spindles were consistently aligned parallel to the
452 epithelial sheet (Fig. 4K, K'; N=35).

453 Mitotic cell rounding and cytokinesis employ processes that reorganize the cytoskeleton,
454 generating forces that locally affect cell rearrangement and tissue morphogenesis (Champion et
455 al., 2017, Pinheiro and Bellaïche, 2018). We observed an increase in F-actin along the apical
456 junctions in PH3-positive SG cells (Fig. 4L). Increased F-actin signals were also often detected
457 along the apical-lateral membrane in PH3-positive cells and along the entire membrane of cells
458 in prophase (data not shown). While no biased distribution of dividing cells was observed across
459 the SG placode in *hkb* mutants, dividing cells were more frequently localized in the outer domain
460 (50% of the placode radius) compared to the inner domain (Fig. 4N, O). SG-specific expression
461 of Hkb in *hkb* mutants reduced the number of PH3-positive cells significantly (Fig. 4I, M),
462 suggesting a role for Hkb in inhibiting the mitotic entry of SG cells.

463 Given that apoptosis can induce compensatory cell proliferation in neighboring cells to maintain
464 tissue homeostasis (Haynie and Bryant, 1977, Kondo et al., 2006, Crucianelli et al., 2022), we
465 investigated whether the abnormal cell division in *hkb* mutants was a result of apoptosis. We
466 observed PH3 signals in p35-overexpressing SGs in *hkb* mutants, comparable to those in *hkb*
467 mutants alone (Fig. 4J, M). We conclude that the abnormal cell division in *hkb* mutants is not
468 compensatory cell proliferation induced by apoptosis.

469

470 **Hkb regulates endoreplication progression during SG morphogenesis**

471 The observation of cell division in SG cells was unexpected because SG cells do not divide but
472 rather undergoe endoreplication. To further test the cell cycle status in SG cells, we used the Fly-
473 FUCCI system, which allows for the identification of the different cell cycle phases based on the
474 fluorescent signals of cyclin B (CycB) and E2F transcription factor 1 (E2F1)-tagged degrons
475 ((Zielke et al., 2014); Fig. 5A). Prior to invagination at early stage 11, all WT SG cells exhibited
476 strong nuclear signals for E2F1 and cytoplasmic signals for CycB (Fig. 5B-B''), indicating G2
477 phase. During late stage 11 and stage 12, distal SG cells that had completed invagination showed
478 reduced E2F1 signals and very low levels of CycB (Fig. 5D-D''), and by stage 13, nuclear E2F1
479 signals were almost completely lost in all SG cells, accompanied by low levels of CycB (Fig. 5F-
480 F''). These data indicate a distal-to-proximal transition to S phase, consistent with a previous
481 finding using BrdU staining (Chandrasekaran and Beckendorf, 2005). At late stage 13, distal SG
482 cells began to exhibit weak E2F1 signals (data not shown), and by stage 14, most SG cells
483 regained E2F1 signals except for a few proximal cells (Fig. 5H-H''), indicating a distal-to-
484 proximal transition to G2 phase. During stages 15 and 16, except for a few randomly placed
485 cells, all SG cells accumulated E2F1 signals along with increased CycB expression (Fig. 5J-J'').
486 Our data suggest a distal-to-proximal wave of endoreplication progression during normal SG
487 morphogenesis.

488 In *hkb* mutant SGs, the distal-to-proximal progression of endoreplication was disrupted. Similar
489 to WT, most cells in early stage 11 *hkb* mutant SGs exhibited strong nuclear signals for E2F1
490 and cytoplasmic CycB signals (Fig. 5C-C''), except in dividing cells where CycB signals were
491 distributed throughout the entire cell (red arrowheads in Fig. 5C''), which is consistent with the

492 distribution of CycB during mitosis (Jackman et al., 1995). However, from late stage 11 to stage
493 14, almost all SG cells in *hkb* mutants showed nuclear E2F1 signals in varying intensities (Fig.
494 5E-E'', G-G'', I-I''), suggesting that Hkb plays a critical role in distal-to-proximal
495 endoreplication progression during SG morphogenesis.

496 In both WT and *hkb* mutant embryos at stage 15+, a few SG cells lacked E2F1 signals and
497 showed strong CycB signals (Fig. 5J-J'', K-K''), indicating a possible re-entry into S phase.
498 Although the mechanism underlying this transition remains unclear, we conclude that it is
499 independent of Hkb.

500

501 **Regulation of key cell cycle genes by Hkb is critical for cell survival and SG morphogenesis**

502 To understand the mechanisms of endoreplication regulation during SG morphogenesis, we
503 focused on the direct transcriptional targets of Hkb identified by the modENCODE Project using
504 chromatin immunoprecipitation followed by sequencing (ChIP–seq) on the whole embryo
505 (Consortium et al., 2010). Gene Ontology enrichment analysis revealed several key biological
506 processes associated with the defects observed in *hkb* mutants (Fig. 6A). Notably, gene clusters
507 related to the cell cycle were identified, including central players like *Cyclin A* (*CycA*), *Cyclin D*
508 (*CycD*), *Cyclin E* (*CycE*), *E2F1*, *aurora A* (*aurA*), and *aurora B* (*aurB*). Additionally, several
509 apoptosis-related genes were identified, including *hid*, *rpr*, and *Death related ICE-like caspase*
510 (*Drice*). The full list of Hkb target genes, GO clusters, and the list of genes in each cluster were
511 included in Table S3. Fluorescence in situ hybridization revealed a significant increase in the
512 mRNA levels of *E2F1*, *CycE*, and *rpr* in *hkb* mutant SGs compared to WT at stages 11 and 12
513 (Fig. 6B-G''; Sup. Fig. S11A-B', C-E'', H-I''), suggesting transcriptional repression of these
514 genes by Hkb. *CycA* mRNA levels were increased in some stage 11 SG cells in *hkb* mutants,
515 whereas all WT SG cells of the same stage showed a background level of *CycA* mRNA signals
516 (Sup. Fig. S11F-G').

517 Disruption in cell cycle regulation can lead to apoptosis due to errors in DNA replication or
518 failure of DNA integrity checkpoints (Pucci et al., 2000). Immunostaining with a marker of DNA
519 double-strand breaks (γ-H2Av; (Lake et al., 2013)) showed increased levels in *hkb* mutant SGs

520 compared to WT, indicating increased DNA damage (Sup. Fig. S9). To test whether apoptosis in
521 *hkb* mutant SG cells was triggered by the dysregulation of cell cycle genes, we performed
522 knockdown experiments targeting *CycA* and *CycE* and their interacting Cdk genes (*Cdk1* and
523 *Cdk2*) in *hkb* mutant SGs. Knockdown of *CycA* did not rescue the *hkb* mutant phenotypes (Sup.
524 Fig. S11G). However, knockdown of *CycE* resulted in a reduction in both dividing and dying
525 cells (Fig. 6H, K, N, O), restoring the invagination position and leading to a partial rescue of the
526 short SG phenotypes (Fig. 6H, K; Sup Fig. S10A-D, N). Similar rescue effects were observed
527 with *Cdk1* knockdown (Fig. 6I, L, N, O; Sup. Fig. S10E-H, N). Like SG-specific knockdown,
528 embryos double mutant for *hkb* and *CycE* or *Cdk1* rescued the *hkb* mutant phenotypes, but
529 double mutants for *hkb* and *CycA* did not show significant rescue (Sup. Fig. S11G-M). Embryos
530 singly mutant for *CycA*, *CycD*, *CycE*, and *Cdk1* showed relatively normal morphology except for
531 a few PH3-positive SG cells in *CycD* and *CycE* mutants (Sup. Fig. S11A-D). *Cdk2* mutant
532 embryos showed severe morphological defects with significantly fewer cells overall, making it
533 difficult to assess differences in the *hkb* mutant background (Sup. Fig. S11E, F).

534 To further test Hkb's role in cell cycle regulation, we tested Fizzy-related (Fzr), a cell cycle
535 switch that functions with the anaphase-promoting complex (APC) to degrade mitotic cyclins
536 during M and G1 phases and trigger exit from the M phase (Sigrist and Lehner, 1997). Fzr also
537 regulates the transition from the normal cell cycle to the endocycle by degrading mitotic cyclins
538 during G2 phase (Sigrist and Lehner, 1997, Zielke et al., 2011). We hypothesized that
539 overexpression of Fzr in the *hkb* mutant SG would inhibit cell division, preventing cell death and
540 rescuing the defective tube length phenotype. Supporting our hypothesis, overexpression of Fzr
541 in *hkb* mutant SGs resulted in a reduction in both dividing and dying cells, partially rescuing the
542 overall *hkb* mutant phenotypes (Fig. 6J, M, N, O; Sup Fig. S10I-L, N). These data suggest that
543 the loss of *hkb* leads to the derepression of cyclin/Cdk activities, which disrupts endoreplication
544 and causes SG cells to enter mitosis abnormally (Fig. 7). Consequently, cell death occurs in SG
545 cells, leading to disrupted SG morphology.

546 **Discussion**

547 In this study, we have uncovered a previously uncharacterized role for Hkb in coordinating cell
548 cycle regulation and morphogenesis during development. Through a comprehensive analysis of
549 mutant phenotypes, modENCODE ChIP-Seq targets of Hkb, and genetic interaction analyses, we
550 have revealed the role of Hkb in regulating endoreplication to enable proper development of the
551 SG.

552

553 **Hkb regulates the cell cycle through transcriptional and possibly post-translational**
554 **mechanisms**

555 During *Drosophila* embryonic development, many tissues arrest the cell cycle in the G2 phase
556 after the initial cell divisions (Hartenstein and Campos-Ortega, 1985, Edgar and O'Farrell, 1989).
557 Subsequently, several tissues, including the SG, switch to the endocycle. This switch is
558 correlated with the development of three-dimensional organs, suggesting a metabolic need to
559 inhibit active cell proliferation to allow for such a transition during development. Using the Fly-
560 FUCCI system, we observed progressive endoreplication from distal to proximal regions during
561 normal SG morphogenesis (Fig. 5). Our data are consistent with a previous study showing that
562 distal cells enter S phase first during SG invagination (Chandrasekaran and Beckendorf, 2005).
563 In *hkb* mutant SGs, this progressive endoreplication is lost.

564 We propose that endoreplication in SG cells is regulated, at least in part, by Hkb-mediated
565 transcriptional repression of *CycA*, *CycE*, and *E2F1*(Fig. 6; Sup. Fig. 12). During normal SG
566 development, E2F1 and CycE (which is also a transcriptional target of E2F1; (Ohtani et al.,
567 1995)) may together control the transition to S phase to begin endoreplication. Once transited to
568 S phase, E2F1 activity is repressed. We propose that Hkb promotes SG cell entry into the
569 endocycle through its repression of *E2F1* and *CycE* expression. In support of this, knockdown of
570 *CycE* partially rescued the *hkb* mutant phenotypes (Fig. 6). We also propose that Hkb prevents
571 entry into mitosis, possibly by downregulating *CycA* expression. CycA acts in the S and G2/M
572 transition phases of the cell cycle, where it aids in DNA replication and entry into mitosis by
573 binding to Cdk2 and Cdk1, respectively (Pagano et al., 1992, Yam et al., 2002, Gong and Ferrell

574 Jr, 2010, Bendris et al., 2011). Loss of *hkb* may prevent inhibition of CycA-Cdk1 activity in the
575 SG. In support of this idea, knockdown of *Cdk1*, or overexpression of *Fzr,* an inhibitor of mitotic
576 cyclins, partially rescued the *hkb* mutant phenotypes (Fig. 6). Depletion of the zygotic *CycA* pool
577 did not rescue the *hkb* mutant phenotypes, either because of the contribution of the maternal
578 *CycA* pool or because of the presence of CycB and CycB3, two other cyclins that bind to Cdk1 to
579 regulate mitotic entry.

580 Hkb may regulate the cell cycle not only through transcriptional control of cell cycle genes but
581 also by influencing ubiquitination, a key mechanism of cell cycle regulation. ChIP-Seq analysis
582 revealed that Hkb targets several key components involved in ubiquitination, including *cullin 1*
583 and *archipelago* (*ago*) (Fig. 6A; Table S3). Ago is known to regulate CycE levels in *Drosophila*
584 (Moberg et al., 2001). Remarkably, ZnF transcription factors can interact with both nucleic acids
585 and proteins and are important regulators of protein degradation through ubiquitination (Gibson
586 et al., 1988, Iuchi, 2005). Further studies will provide a deeper understanding of the
587 comprehensive mechanisms by which Hkb regulates the cell cycle.

588

589 **Progressive endoreplication during organ formation**

590 Endoreplication in the *Drosophila* embryonic SG, coupled with invagination, allows cells to
591 increase the number of gene copies to provide sufficient proteins for morphogenesis. The
592 regulatory mechanism behind the progressive distal-to-proximal endoreplicatione in the SG
593 remains unclear. In agreement with Sanchez-Corrales et al., 2021, we observed higher levels of
594 Hkb in the posterior region of the placode at stage 10, which became more uniformly distributed
595 throughout all SG cells by stage 11 (Sup. Fig. S5). The initial difference in Hkb levels within the
596 SG placode may lead to the differential repression of cell cycle genes, contributing to the
597 progression of endoreplication. Alternatively, SG invagination in the dorsal/posterior region
598 could potentially trigger the sequential onset of endoreplication, as suggested by a previous study
599 (Chandrasekaran and Beckendorf, 2005). Further investigation of the relationship between
600 endoreplication regulation and SG invagination will provide a better understanding of how cell
601 cycle and morphogenesis coordinate during organ formation. It will also be interesting to test a

602 role for Hkb in cell cycle (endocycle) regulation in other *Drosophila* tissues, and to test a
603 similarly conserved role for the mammalian SP/KLF transcription factors.

604

605 **Hkb's roles in cytoskeletal reorganization and intracellular trafficking**

606 In line with previous studies on the cellular forces exerted by dividing (Kondo and Hayashi,
607 2013, Pinheiro and Bellaïche, 2018) and apoptotic (Monier et al., 2015, Toyama et al., 2008)
608 cells on neighboring cells, the abnormal cell division and excessive cell death observed in *hkb*
609 mutant SGs are associated with a tissue-wide disruption of actomyosin and cell geometry (Fig.
610 3). Our data show that the centralized invagination phenotype results primarily from excessive
611 cell death (Figs. 2 and 3). However, dividing cells, particularly those near the SG boundary, may
612 contribute to this phenotype by undergoing cell surface area expansion during cell division,
613 increasing the number of cells with larger apical areas along the SG boundary (Fig. 4).

614 Based on Hkb ChIP-Seq targets, we propose that Hkb also plays an active role in regulating
615 cytoskeletal organization through transcriptional regulation of key cytoskeletal regulators. Hkb
616 targets include key Rho signaling components and their regulators, such as the small GTPases
617 Rho1 and Rac1, and several RhoGEFs, including RhoGEF2, a key activator of Rho signaling
618 during epithelial morphogenesis (Barrett et al., 1997) (Fig. 6A; Table S3). We also propose a
619 critical role for Hkb in regulating intracellular trafficking. Supporting previous research on
620 Hkb's role in regulating Klar, an important regulator of intracellular trafficking (Myat and
621 Andrew, 2002), our data show that Rab11 is mislocalized basally in *hkb* mutant SGs (Sup. Fig.
622 S8). Multiple endocytic components, including *βCOP*, *AP-1-2β*, *AP-2α*, and *Nuf*, as well as
623 several Rab GTPases, including *Rab4*, *Rab10*, *Rab27*, and *Rab30*, were also identified as Hkb
624 ChIP-Seq targets (Fig. 6A; Table S3), providing further evidence for the involvement of Hkb in
625 intracellular trafficking. The initial difference in Hkb levels in the SG placode may lead to
626 differential expression of these genes, which could contribute to normal invagination positioning.

627 In conclusion, we have uncovered a role for the Hkb transcription factor in regulating
628 endoreplication and preventing abnormal cell cycle progression during epithelial tube formation.

629 Our findings provide valuable insights into a critical mechanism for coordinating cell cycle
630 regulation and morphogenesis during organ formation.

Acknowledgments

We thank the members of the Chung laboratory for their comments and suggestions. We thank the Bloomington *Drosophila* Stock Center for fly stocks, and D. J. Andrew and the Developmental Studies Hybridoma Bank for antibodies. We thank Flybase and the modENCODE transcription consortium for the gene information and the Hkb ChIP-Seq data. We are grateful to J. C. Larkin and J. L. Woodward for their helpful comments on the manuscript. Cartoons in Figures 1, 5 and 7 were created using Biorender.com. This work was supported by a start-up fund from Louisiana State University and grants from the Louisiana Board of Regents Research Competitiveness Subprogram and the National Science Foundation (MCB 2141387) to S.C.

Fig 1.

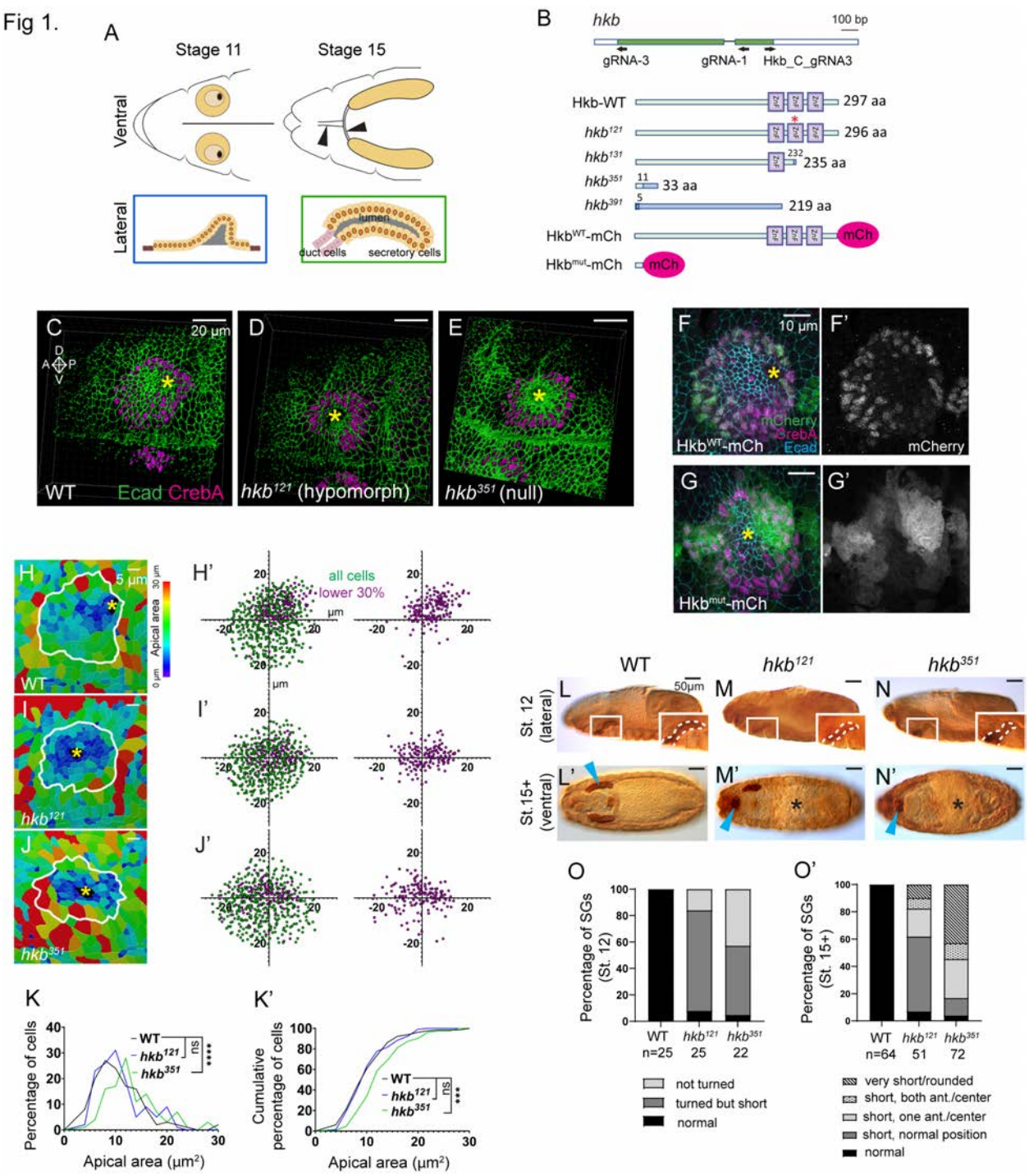

Figure 1. Generation of new *hkb* alleles and fluorescent knock-in lines. (A) Top cartoon diagram: Anterior region of stage 11 and 15 *Drosophila* embryos. SGs shown in yellow. Brown area, clustered apical constriction of SG cells during invagination. Black, invagination pit.

Arrowheads, salivary duct. Bottom cartoon diagram: Lateral view of SG at stages 11 and 15. Orange circles, SG cell nuclei. Gray, SG lumen. (B) Top cartoon diagram: *hkb* transcript displayed with coding exon in green and gRNAs used for *hkb* alleles and mCh knock-in lines. Bottom: Hkb protein structures produced in each allele and knock-in lines. In hkb^{121}, two amino acids (N237 and E238) are substituted with K237 (asterisk). In hkb^{351} and hkb^{391}, a short N-terminal region of the Hkb protein (green) is followed by random amino acid sequences (blue) due to a frameshift. *hkb* mRNA with the premature stop codon in hkb^{351} might be degraded by nonsense-mediated mRNA decay. ZnF, zinc finger domain. (C-E) 3D reconstruction of the confocal images of invaginating SGs immunolabeled with Ecad and CrebA. Asterisks, invagination pit. (F-G') Confocal images of stage 11 SGs immunostained for mCh (green), CrebA (magenta), and Ecad (cyan). (H-J) Heat maps showing apical area distribution in invaginating SGs. (H'-J') Scatter plots showing the relative position of cells in the SG placode. X and Y axes represent the distance along the A/P and D/V axes, respectively, from the center of the placode. Cells in the bottom 30% of the apical area (magenta) and all cells (green) are plotted. (K, K') Quantification of the apical area distribution in SG cells. Mann-Whitney U test (percentage of cells) and Kolmogorov-Smirnov test (cumulative percentage of cells). N=5 (WT, 572 cells; hkb^{121}, 505 cells; hkb^{351}, 498 cells). **, $p<0.05$; ***, $p<0.005$; ****, $p<0.0005$. (L-N') Embryos immunostained for CrebA, with magnified views (insets) showing SGs outlined by white dashed lines. Cyan arrowheads, late-stage SGs. Asterisks, defective gut morphology. (O, O') Quantification of the phenotypic distribution of SGs. n, number of embryos. Statistical significance determined using two-way ANOVA.

Fig 2.

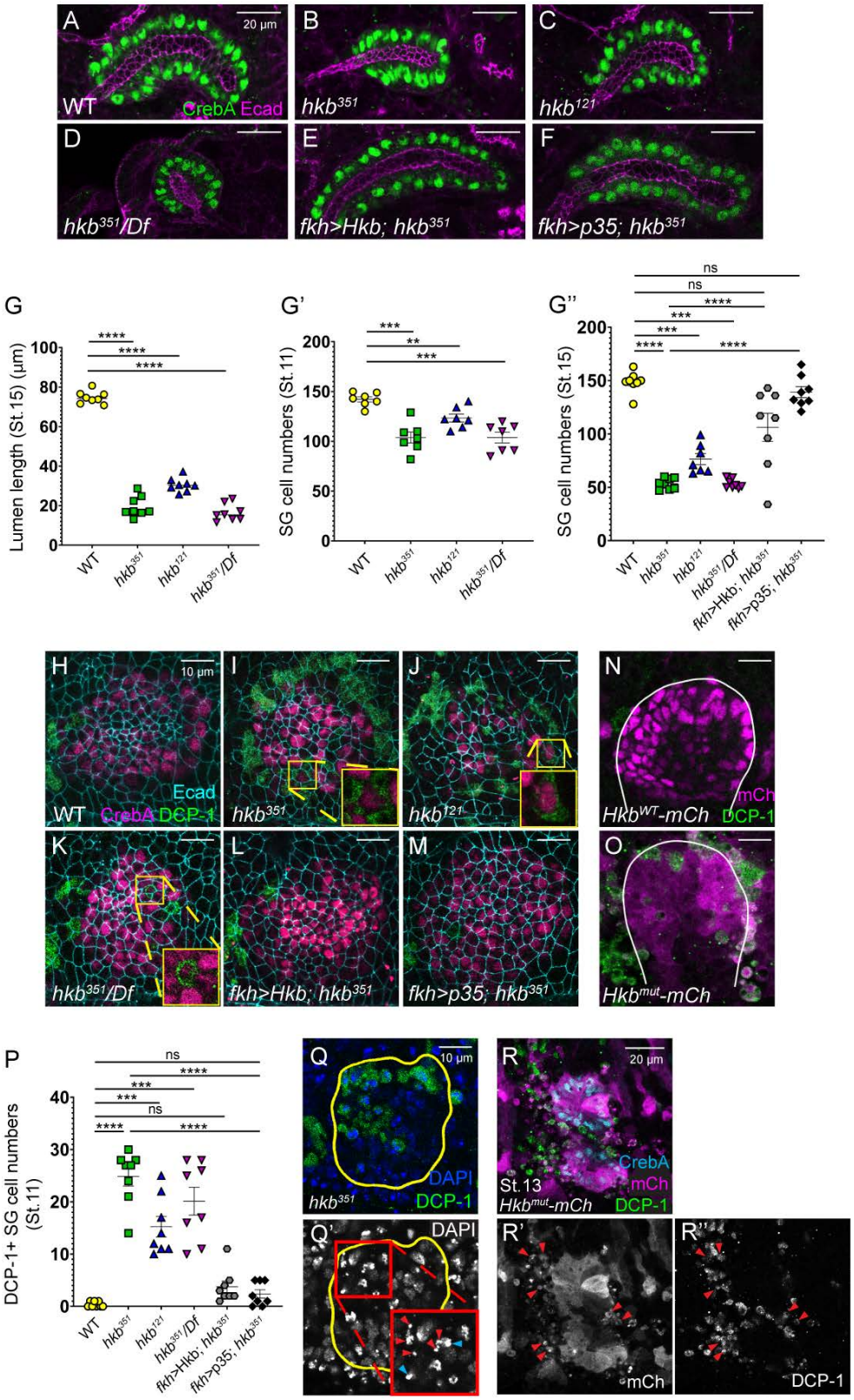
A
20 µm
WT
CrebA Ecad
B
hkb351
C
hkb121
D
hkb351/Df
E
fkh>Hkb; hkb351
F
fkh>p35; hkb351
G
Lumen length (St.15) (µm)
WT
hkb351
hkb121
hkb351/Df
G'
SG cell numbers (St.11)
G''
SG cell numbers (St.15)
fkh>Hkb; hkb351
fkh>p35; hkb351
H
10 µm
Ecad
WT
CrebA DCP-1
I
J
N
mCh
HkbWT-mCh
DCP-1
K
L
M
O
Hkbmut-mCh
P
DCP-1+ SG cell numbers (St.11)
Q
DAPI
DCP-1
Q'
R
CrebA
St.13
mCh
R'
mCh
R''
DCP-1

669

670 **Figure 2. Hkb is required to prevent apoptosis in SG cells.** (A-F) Stage 15+ SGs
671 immunolabeled for Ecad (magenta) and CrebA (green). (G) Quantification of the stage 15+ SG
672 lumen length. N=9 (WT), 12 (*hkb*^{351}), 11 (*hkb*^{121}), and 8 (*hkb*^{351}/*Df*). One-way ANOVA. ****,
673 $p<0.0005$. (G'-G'') Quantification of the number of SG secretory cells at stage 11 (G'; N=7 for
674 all genotypes) and stage 15 (G''; N=8 for all genotypes except *hkb*^{121} (N=7)). One-way
675 ANOVA. **, $p<0.05$; ***, $p<0.005$; ****, $p<0.0005$. (H-M) Pre-invaginating SGs
676 immunolabeled for DCP-1 (green), CrebA (magenta), and Ecad (cyan). Insets, magnified views.
677 (N, O) Hkb^{WT}-mCh and Hkb^{mut}-mCh SGs immunostained for mCh (magenta) and DCP-1
678 (green). White lines, SG boundary. (P) Quantification of the DCP-1 positive SG cells. N=8 for
679 all genotypes. One-way ANOVA. ***, $p<0.005$; ****, $p<0.0005$. (Q, Q') Stage 11 *hkb* null
680 mutant SG stained for DAPI (blue) and DCP-1 (green). Insets, higher magnification of the red-
681 boxed region. Red arrowheads, fragmented nuclei. Cyan arrowheads, pyknotic nuclei. Yellow
682 lines, SG boundary. (R-R'') SG of a stage 13 Hkb^{mut}-mCh embryo immunostained for mCh
683 (cyan), CrebA (magenta), and DCP-1 (green). Arrowheads, mCh- and DCP-1-positive cells near
684 the SG.

685

Fig 3.

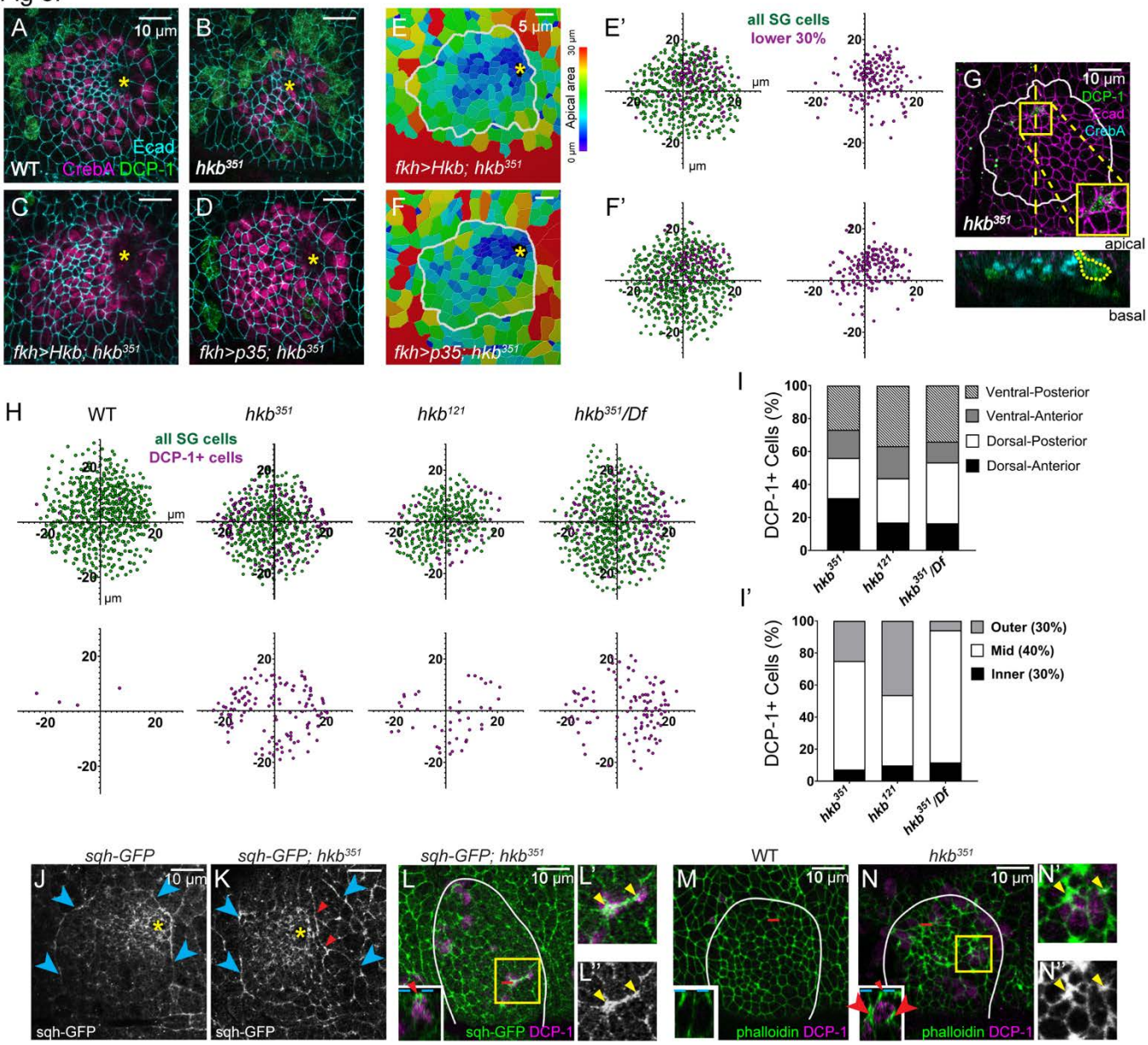

686

687 **Figure 3. Aberrant cell death results in centered invagination in the *hkb* mutant SG.** (A-D)
688 Sstage 11 SGs immunolabeled with DCP-1 (green), CrebA (magenta), and Ecad (cyan). (E-F)
689 Heat maps depicting apical area distribution in invaginating SGs. (E'-F') Scatter plots showing
690 the relative position of cells in the SG placode. X and Y axes represent the distance along the
691 A/P and D/V axes, respectively, from the center of the placode. Cells in the bottom 30% of the
692 apical area (magenta) and all cells (green) are plotted. (G) *hkb* mutant SG immunostained for
693 DCP-1 (green), Ecad (magenta), and CrebA (cyan). Insets, magnified view of the yellow boxed

694 regions. Z-section along the dotted line displayed below. (H) Scatter plots showing the relative
695 position of total SG cells (green) and DCP-1-positive cells (magenta) in stage 11 SGs. (I, I')
696 Quantification of the number of DCP-1-positive SG cells in different regions of the placode. (J,
697 K) Stage 11 SGs immunostained for GFP (for *sqh-GFP*). Cyan arrowheads, supracellular myosin
698 cable. Red arrowheads, short cables inside the SG placode. Yellow asterisk, invagination pit. (L-
699 L'') Stage 11 SGs immunostained for GFP (for *sqh-GFP*; green) and DCP-1 (magenta). (M-N'')
700 Stage 11 SGs stained for F-actin (green) and DCP-1 (magenta). Insets in L-N, z-sections along
701 red dotted lines. Dotted cyan lines, apical boundary of cells. Red arrowheads/arrows indicate
702 increased myosin (L) and F-actin (N) signals in the apical and lateral regions of the DCP-1-
703 positive cell, respectively. (L', L'', N', N'') Magnified views of yellow boxed regions in L and
704 N. Yellow arrowheads, increased myosin/F-actin signals at the apical-junctional region of DCP-
705 1-positive cells.

706

Fig 4.

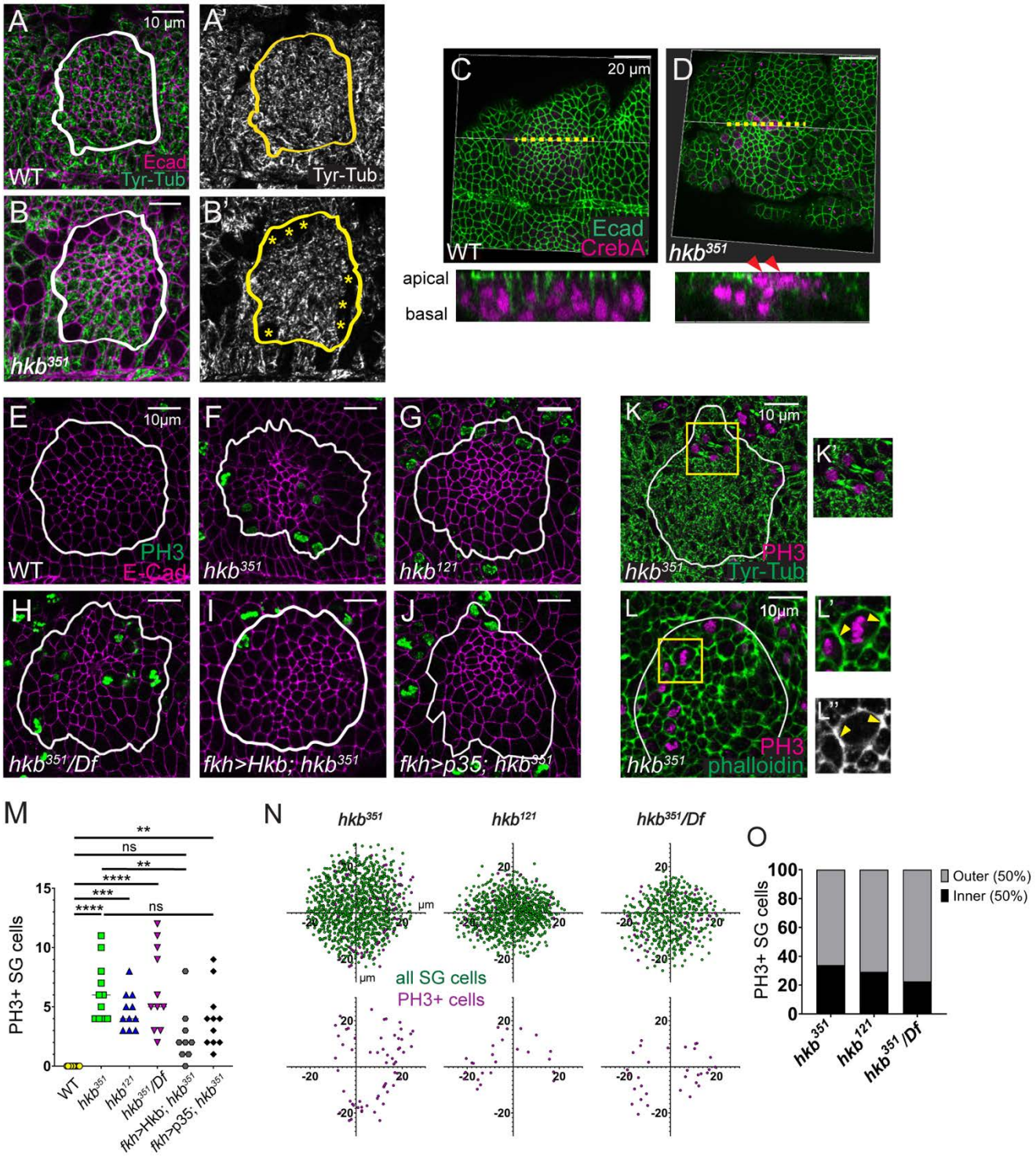

Figure 4. SG cells undergo abnormal cell division in *hkb* mutants. (A-B') Stage 11 SGs immunolabeled with Tyr-Tub (green) and Ecad (magenta). White and yellow lines, SG

710 boundary. Asterisks, cells without Tyr-Tub signals. (C, D) 3D reconstructions of confocal
711 images of pre-invaginating SGs immunolabeled with Ecad (green) and CrebA (magenta). Z-
712 sections along yellow dotted lines shown below. Arrowheads, apically localizing nuclei in *hkb*
713 mutant SG. (E-J) Stage 11 SGs immunolabeled with PH3 (green) and Ecad (magenta). White
714 lines, SG boundary. (K, K') Stage 11 SGs immunolabeled with Tyr-Tub (green) and PH3
715 (magenta). Higher magnification of yellow boxed region shown in K'. White lines, SG
716 boundary. (L-L'') Stage 11 SGs immunolabeled with PH3 (magenta) and phalloidin (green).
717 Higher magnification of yellow boxed region shown in L' and L''. White lines, SG boundary.
718 (M) Quantification of the number of PH3-positive SG cells. N=11 for all genotypes except
719 *fkh*>Hkb; hkb^{351}(N=9). One-way ANOVA. **, $p<0.05$; ***, $p<0.005$; ****, $p<0.0005$. (N)
720 Scatter plots showing the position of total SG cells (green) and PH3-positive cells (magenta) in
721 the SG placode. X and Y axes represent the distance along the A/P and D/V axes, respectively,
722 from the center of the placode. (O) Quantification of the number of PH-positive SG cells in
723 different regions of the placode.

724

Fig 5.

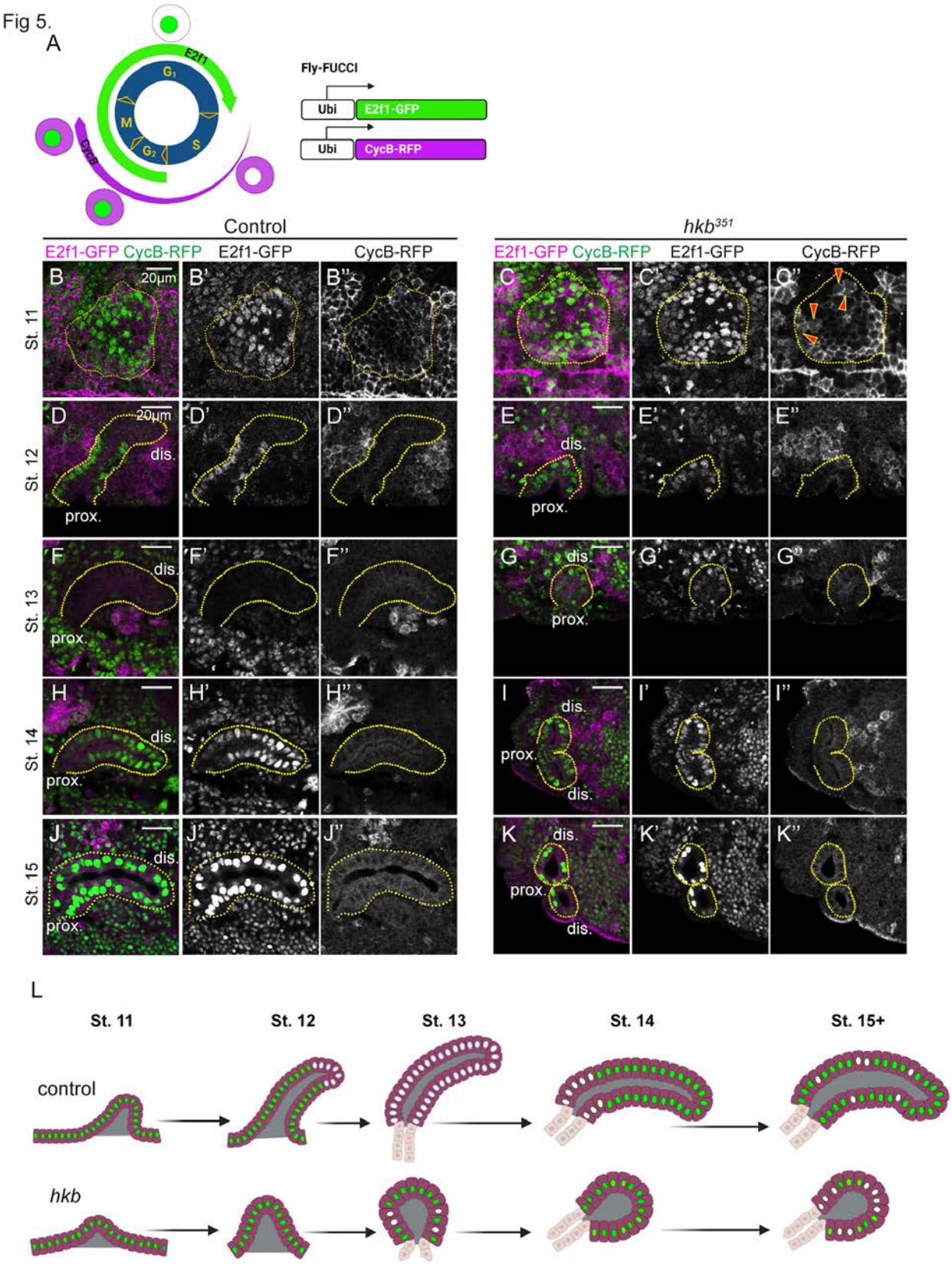
A
E2f1
G1
M
G2
S
CycB
Fly-FUCCI
Ubi
E2f1-GFP
Ubi
CycB-RFP
Control
hkb351
E2f1-GFP CycB-RFP
E2f1-GFP
CycB-RFP
St. 11
St. 12
St. 13
St. 14
St. 15
20µm
dis.
prox.
L
St. 11
St. 12
St. 13
St. 14
St. 15+
control
hkb

725

726 **Figure 5. The distal-to-proximal progression of the endoreplication is disrupted in the *hkb***
727 **mutant SG.** (A) Schematic of the Fly-FUCCI system. (B-K'') SGs immunolabeled with GFP
728 (for E2F1-GFP; green) and CycB (for CycB-RFP; magenta) at different stages. Red arrowheads
729 in C'', CycB signals distributed throughout the dividing cells. Yellow dotted lines, SG boundary.
730 dis. denotes distal; prox. denotes proximal. (L) Summary of cell cycle status in SG cells during
731 development.

732

Fig 6.

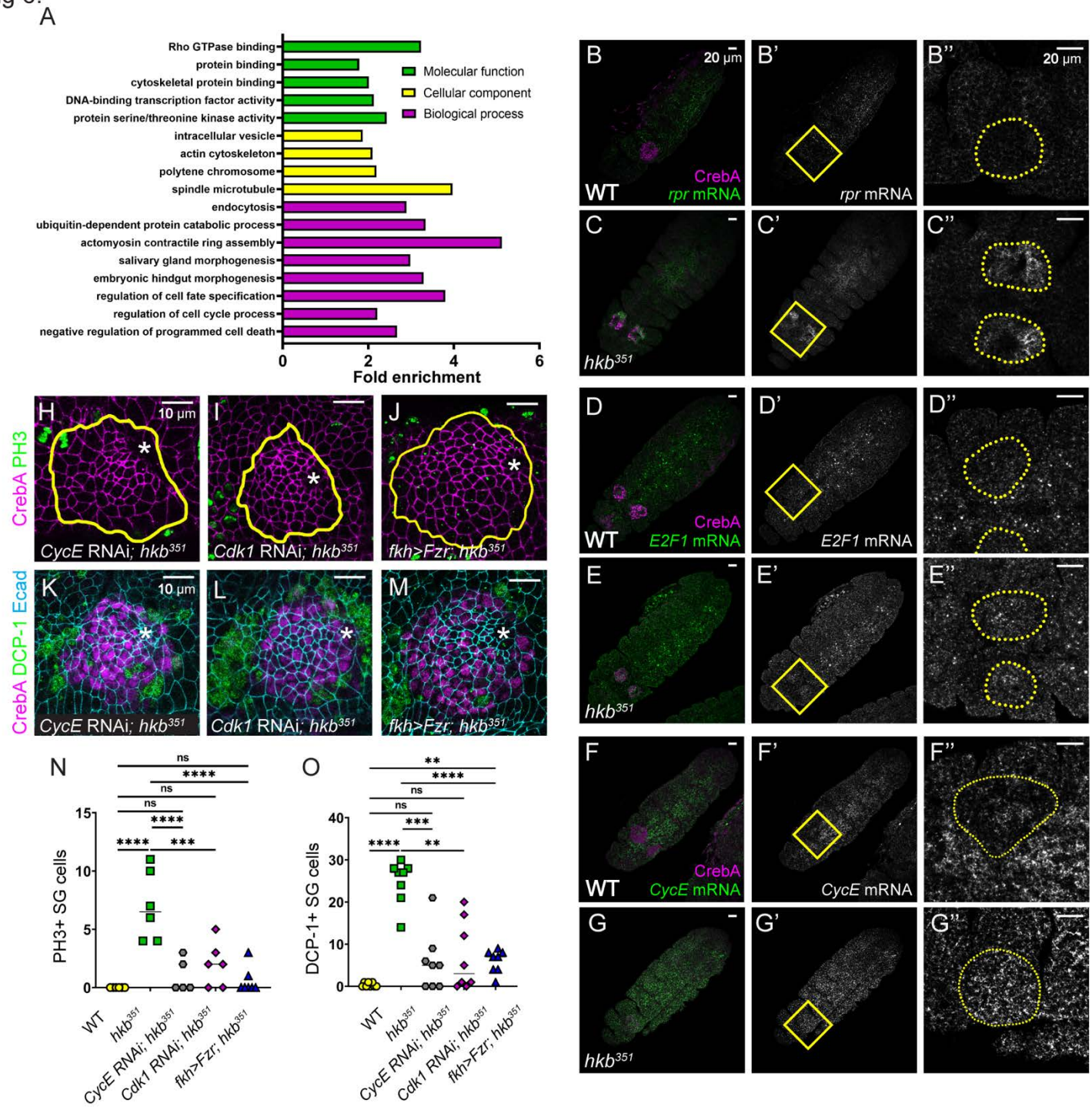

733

734 **Figure. 6. Hkb regulates key cell cycle and cell death genes transcriptionally .** (A) GO
735 enrichment analysis of ModENCODE Hkb ChIP-Seq data. (B-E'') Fluorescence *in situ*
736 hybridization images of stage 11 embryos showing mRNA levels of *rpr* (B-C''), *E2F1* (D-E''),

737 and *CycE* (F-G''). Yellow boxed regions shown at a higher magnification in B''-G''. (H-M)
738 *Cdk1* and *CycE* knockdowns and Fzr overexpression in *hkb* mutant SGs immunostained for Ecad
739 (magenta) and PH3 (green) (H-J) and Ecad (magenta), DCP-1 (green), and CrebA (cyan) (K-M).
740 Yellow lines, SG boundary. Asterisks, invagination pit. (N, O) Quantification of the number of
741 PH3-positive (N) and DCP-1-positive (O) SG cells. N=6 (N) and 8 (O) for all genotypes. One-
742 way ANOVA. **, $p<0.05$; ***, $p<0.005$; ****, $p<0.0005$.

743

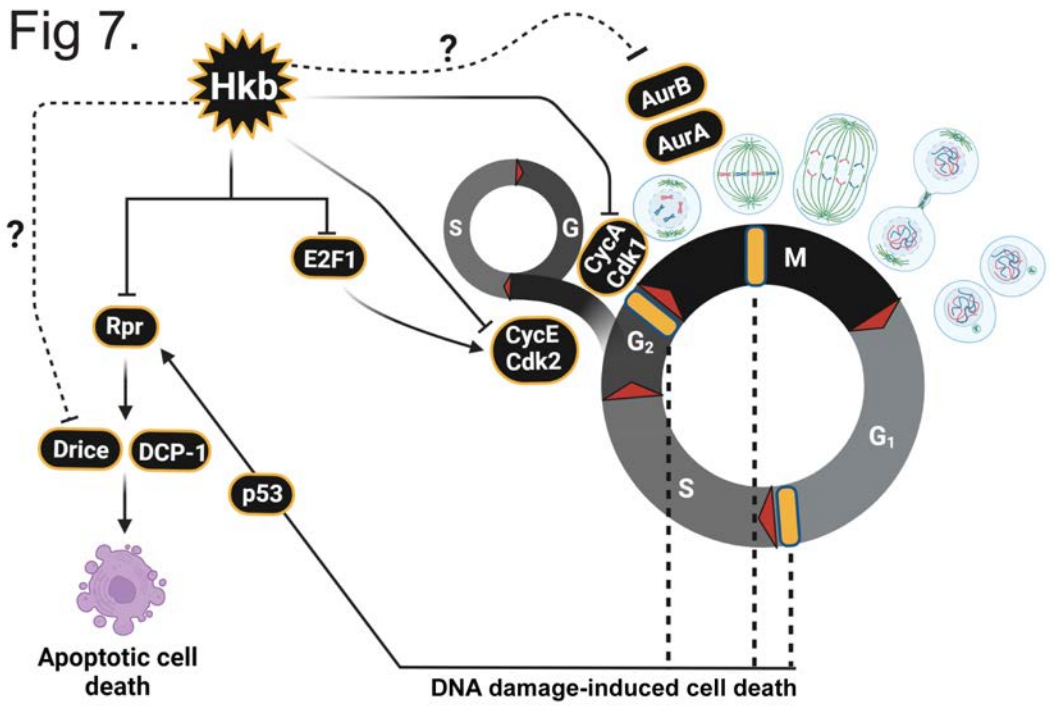

744

745

746 **Figure 7. A model for endoreplication regulation by Hkb during SG morphogenesis.**

747

748 **Table S1. Fly strains used**

Fly strain	**Sources and References**	**RRID**
Oregon R (wild type)		
fkh-Gal4	Henderson and Andrew, 2000	BDSC_78060
hkb^{121}	This study	
hkb^{131}	This study	
hkb^{351}	This study	
hkb^{391}	This study	
Hkb^{WT}*-mCh*	This study	
Hkb^{mut}*-mCh*	This study	
hkb^{2}	Weigel et al., 1990	
hkb^{A321R1}	Gaul and Weigel, 1991	
UAS-p35		BDSC_5072
UAS-Hkb	Myat and Andrew, 2002	
$CycE^{AR95}$		BDSC_6637
$CycD^{1}$		BDSC_55125
$CycA^{C8LR1}$		BDSC_6627
$Cdk1^{B47}$		BDSC_6643
TRiP.GL00511 (UAS-CycE RNAi)		BDSC_36092
TRiP.HMS01531 (*UAS-Cdk1 RNAi*)		BDSC_36117

UAS-Fzr		BDSC_91688
Ubi-GFP.E2f1, Ubi-mRFP1.CycB		BDSC_55098

749

750 **Table S2. Antibodies Used**

Antibody	Source	RRID	Dilution
α-Ecad (rat)	DSHB (DCAD2)	AB_528120	1:50
α-CrebA (rat)	Andrew lab (John Hopkins University); re-made in this study		1:3,000
α-CrebA (rabbit)	Andrew lab (John Hopkins University)	AB_10805295	1:5,000
α-CrebA (guinea pig)	This study		1:5,000
α-GFP (mouse)	Invitrogen (A11120)	AB_221568	1:500
α-GFP (chicken)	Invitrogen (A10262)	AB_2534023	1:1,000
α-RFP (rabbit)	Invitrogen (R10367)	AB_10563941	1: 2,000
α-β-galactosidase (rabbit)	Invitrogen (A11132)	AB_221539	1:500
α-β-galactosidase (mouse)	Invitrogen (MA5-15222)	AB_10980770	1:500
α-mCherry (rat)	Invitrogen (M11217)	AB_2536611	1:1,000
α-mCherry (rabbit)	Invitrogen (PA534974)	AB_2552323	1:1,000
α-DCP-1 (rabbit)	Cell signaling technology (9578)	AB_2721060	1:200
α-phosphohistone 3 (rabbit)	Invitrogen (PA517869)	AB_10984484	1:1,000
α-tyrosinated α-tubulin (rat)	Invitrogen (MA1-80017)	AB_2210201	1:1,000
α-H2AvD (mouse)	DSHB (UNC93-5.2.1)	AB_2618077	1: 1,000

α-Sage (guinea pig)	Andrew lab (Johns Hopkins University)		1: 100
α-CyclinB (mouse)	DSHB (F2F4)	AB_528189	1: 5
α-Crb (mouse)	DSHB (Cq4)	AB_528181	1:10
α-Rab11 (rabbit)	Andrew lab (John Hopkins University)		1:500
α-mCherry (rat)	Invitrogen (M11217)	AB_2536611	1:1,000
α-mCherry (rabbit)	Invitrogen (PA534974)	AB_2552323	1:1,000
α-α-Spectrin (mouse)	DSHB (3A9)	AB_528473	1:2
α-Dead Ringer (chicken)	Andrew lab (Johns Hopkins University)		1:1000
Phalloidin Alexa 488	Invitrogen (A12379)		1:250
Alexa Fluor 488/568/647-coupled secondary antibodies	Invitrogen		1:500

751

References

ANDREW, D. J. & EWALD, A. J. 2010. Morphogenesis of epithelial tubes: Insights into tube formation, elongation, and elaboration. *Developmental biology,* 341**,** 34-55.

BAENA-LOPEZ, L. A., ALEXANDRE, C., MITCHELL, A., PASAKARNIS, L. & VINCENT, J.-P. 2013. Accelerated homologous recombination and subsequent genome modification in Drosophila. *Development,* 140**,** 4818-4825.

BARRETT, K., LEPTIN, M. & SETTLEMAN, J. 1997. The Rho GTPase and a putative RhoGEF mediate a signaling pathway for the cell shape changes in Drosophila gastrulation. *Cell,* 91**,** 905-915.

BENDRIS, N., LEMMERS, B., BLANCHARD, J.-M. & ARSIC, N. 2011. Cyclin A2 mutagenesis analysis: a new insight into CDK activation and cellular localization requirements. *PloS one,* 6**,** e22879.

BOOTH, A. J., BLANCHARD, G. B., ADAMS, R. J. & RÖPER, K. 2014. A dynamic microtubule cytoskeleton directs medial actomyosin function during tube formation. *Developmental cell,* 29**,** 562-576.

BRÖNNER, G., CHU-LAGRAFF, Q., DOE, C. Q., COHEN, B., WEIGEL, D., TAUBERT, H. & JÄCKLE, H. 1994. Sp1/egr-like zinc-finger protein required for endoderm specification and germ-layer formation in Drosophila. *Nature,* 369**,** 664-668.

CHAMPION, L., LINDER, M. I. & KUTAY, U. 2017. Cellular reorganization during mitotic entry. *Trends in cell biology,* 27**,** 26-41.

CHANDRASEKARAN, V. & BECKENDORF, S. K. 2003. senseless is necessary for the survival of embryonic salivary glands in Drosophila. *Development,* 130**,** 4719-4728.

CHANDRASEKARAN, V. & BECKENDORF, S. K. 2005. Tec29 controls actin remodeling and endoreplication during invagination of the Drosophila embryonic salivary glands.

CHUNG, S., HANLON, C. D. & ANDREW, D. J. 2014. Building and specializing epithelial tubular organs: the Drosophila salivary gland as a model system for revealing how epithelial organs are specified, form and specialize. *Wiley Interdisciplinary Reviews: Developmental Biology,* 3**,** 281-300.

CHUNG, S., KIM, S. & ANDREW, D. J. 2017. Uncoupling apical constriction from tissue invagination. *Elife,* 6**,** e22235.

CONSORTIUM, M., ROY, S., ERNST, J., KHARCHENKO, P. V., KHERADPOUR, P., NEGRE, N., EATON, M. L., LANDOLIN, J. M., BRISTOW, C. A. & MA, L. 2010. Identification of functional elements and regulatory circuits by Drosophila modENCODE. *Science,* 330**,** 1787-1797.

CRUCIANELLI, C., JAISWAL, J., VIJAYAKUMAR MAYA, A., NOGAY, L., COSOLO, A., GRASS, I. & CLASSEN, A.-K. 2022. Distinct signaling signatures drive compensatory proliferation via S-phase acceleration. *PLoS Genetics,* 18**,** e1010516.

DURONIO, R. J., O'FARRELL, P. H., XIE, J.-E., BROOK, A. & DYSON, N. 1995. The transcription factor E2F is required for S phase during Drosophila embryogenesis. *Genes & development,* 9**,** 1445-1455.

EDGAR, B. A. & O'FARRELL, P. H. 1989. Genetic control of cell division patterns in the Drosophila embryo. *Cell,* 57**,** 177-187.

FOLLETTE, P. J., DURONIO, R. J. & O'FARRELL, P. H. 1998. Fluctuations in cyclin E levels are required for multiple rounds of endocycle S phase in Drosophila. *Current Biology,* 8**,** 235-238.

797 FOX, R. M., VAISHNAVI, A., MARUYAMA, R. & ANDREW, D. J. 2013. Organ-specific
798 gene expression: the bHLH protein Sage provides tissue specificity to Drosophila FoxA.
799 *Development,* 140**,** 2160-2171.
800 GANDARILLAS, A., MOLINUEVO, R. & SANZ-GÓMEZ, N. 2018. Mammalian
801 endoreplication emerges to reveal a potential developmental timer. *Cell Death &*
802 *Differentiation,* 25**,** 471-476.
803 GAUL, U. & WEIGEL, D. 1990. Regulation of Krüppel expression in the anlage of the
804 Malpighian tubules in the Drosophila embryo. *Mechanisms of development,* 33**,** 57-67.
805 GIBSON, T. J., POSTMA, J. P., BROWN, R. S. & ARGOS, P. 1988. A model for the tertiary
806 structure of the 28 residue DNA-binding motif ('zinc finger') common to many
807 eukaryotic transcriptional regulatory proteins. *Protein Engineering, Design and*
808 *Selection,* 2**,** 209-218.
809 GIRDLER, G. C. & RÖPER, K. Controlling cell shape changes during salivary gland tube
810 formation in Drosophila. Seminars in Cell & Developmental Biology, 2014. Elsevier,
811 74-81.
812 GODARD, B. G. & HEISENBERG, C.-P. 2019. Cell division and tissue mechanics. *Current*
813 *opinion in cell biology,* 60**,** 114-120.
814 GONG, D. & FERRELL JR, J. E. 2010. The roles of cyclin A2, B1, and B2 in early and late
815 mitotic events. *Molecular biology of the cell,* 21**,** 3149-3161.
816 GREGORY, S. L., KORTSCHAK, R. D., KALIONIS, B. & SAINT, R. 1996. Characterization
817 of the dead ringer gene identifies a novel, highly conserved family of sequence-specific
818 DNA-binding proteins. *Molecular and cellular biology,* 16**,** 792-799.
819 GURLEY, L. R., D'ANNA, J. A., BARHAM, S. S., DEAVEN, L. L. & TOBEY, R. A. 1978.
820 Histone phosphorylation and chromatin structure during mitosis in Chinese hamster cells.
821 *European journal of biochemistry,* 84**,** 1-15.
822 HARTENSTEIN, V. & CAMPOS-ORTEGA, J. A. 1985. Fate-mapping in wild-type Drosophila
823 melanogaster: I. The spatio-temporal pattern of embryonic cell divisions. *Wilhelm Roux's*
824 *archives of developmental biology,* 194**,** 181-195.
825 HAYNIE, J. L. & BRYANT, P. J. 1977. The effects of X-rays on the proliferation dynamics of
826 cells in the imaginal wing disc of Drosophila melanogaster. *Wilhelm Roux's archives of*
827 *developmental biology,* 183**,** 85-100.
828 HENDERSON, K. D. & ANDREW, D. J. 2000. Regulation and function of Scr, exd, and hth in
829 the Drosophila salivary gland. *Developmental biology,* 217**,** 362-374.
830 HERRIGES, M. & MORRISEY, E. E. 2014. Lung development: orchestrating the generation
831 and regeneration of a complex organ. *Development,* 141**,** 502-513.
832 HUH, J. R., GUO, M. & HAY, B. A. 2004. Compensatory proliferation induced by cell death in
833 the Drosophila wing disc requires activity of the apical cell death caspase Dronc in a
834 nonapoptotic role. *Current Biology,* 14**,** 1262-1266.
835 ISMAT, A., CHESHIRE, A. M. & ANDREW, D. J. 2013. The secreted AdamTS-A
836 metalloprotease is required for collective cell migration. *Development,* 140**,** 1981-1993.
837 IUCHI, S. 2005. C2H2 zinc fingers as DNA binding domains. *Zinc finger proteins: From atomic*
838 *contact to cellular function.* Springer.
839 JACKMAN, M., FIRTH, M. & PINES, J. 1995. Human cyclins B1 and B2 are localized to
840 strikingly different structures: B1 to microtubules, B2 primarily to the Golgi apparatus.
841 *The EMBO journal,* 14**,** 1646-1654.

842 KO, C. S., TSERUNYAN, V. & MARTIN, A. C. 2019. Microtubules promote intercellular
843 contractile force transmission during tissue folding. *Journal of Cell Biology,* 218**,** 2726-
844 2742.
845 KONDO, S., SENOO-MATSUDA, N., HIROMI, Y. & MIURA, M. 2006. DRONC coordinates
846 cell death and compensatory proliferation. *Molecular and cellular biology,* 26**,** 7258-
847 7268.
848 KONDO, T. & HAYASHI, S. 2013. Mitotic cell rounding accelerates epithelial invagination.
849 *Nature,* 494**,** 125-129.
850 LAKE, C. M., KORDA HOLSCLAW, J., BELLENDIR, S. P., SEKELSKY, J. & HAWLEY, R.
851 S. 2013. The development of a monoclonal antibody recognizing the Drosophila
852 melanogaster phosphorylated histone H2A variant (γ-H2AV). *G3: Genes, Genomes,*
853 *Genetics,* 3**,** 1539-1543.
854 LE, T. P. & CHUNG, S. 2021. Regulation of apical constriction via microtubule-and Rab11-
855 dependent apical transport during tissue invagination. *Molecular Biology of the Cell,* 32**,**
856 1033-1047.
857 LEGOFF, L. & LECUIT, T. 2015. Mechanical forces and growth in animal tissues. Cold Spring
858 Harb. Perspect. Biol. 8, a019232.
859 MAO, Y., TOURNIER, A. L., HOPPE, A., KESTER, L., THOMPSON, B. J. & TAPON, N.
860 2013. Differential proliferation rates generate patterns of mechanical tension that orient
861 tissue growth. *The EMBO journal,* 32**,** 2790-2803.
862 MARINARI, E., MEHONIC, A., CURRAN, S., GALE, J., DUKE, T. & BAUM, B. 2012. Live-
863 cell delamination counterbalances epithelial growth to limit tissue overcrowding. *Nature,*
864 484**,** 542-545.
865 MARUYAMA, R., GREVENGOED, E., STEMPNIEWICZ, P. & ANDREW, D. J. 2011.
866 Genome-wide analysis reveals a major role in cell fate maintenance and an unexpected
867 role in endoreduplication for the Drosophila FoxA gene Fork head. *PloS one,* 6**,** e20901.
868 MASSA, V., SAVERY, D., YBOT-GONZALEZ, P., FERRARO, E., RONGVAUX, A.,
869 CECCONI, F., FLAVELL, R., GREENE, N. D. & COPP, A. J. 2009. Apoptosis is not
870 required for mammalian neural tube closure. *Proceedings of the National Academy of*
871 *Sciences,* 106**,** 8233-8238.
872 MONIER, B., GETTINGS, M., GAY, G., MANGEAT, T., SCHOTT, S., GUARNER, A. &
873 SUZANNE, M. 2015. Apico-basal forces exerted by apoptotic cells drive epithelium
874 folding. *Nature,* 518**,** 245-248.
875 MYAT, M. M. & ANDREW, D. J. 2000a. Fork head prevents apoptosis and promotes cell shape
876 change during formation of the Drosophila salivary glands. *Development,* 127**,** 4217-
877 4226.
878 MYAT, M. M. & ANDREW, D. J. 2000b. Organ shape in the Drosophila salivary gland is
879 controlled by regulated, sequential internalization of the primordia. *Development,* 127**,**
880 679-691.
881 MYAT, M. M. & ANDREW, D. J. 2002. Epithelial tube morphology is determined by the
882 polarized growth and delivery of apical membrane. *Cell,* 111**,** 879-891.
883 NIKOLOPOULOU, E., GALEA, G. L., ROLO, A., GREENE, N. D. & COPP, A. J. 2017.
884 Neural tube closure: cellular, molecular and biomechanical mechanisms. *Development,*
885 144**,** 552-566.

886 OHTANI, K., DEGREGORI, J. & NEVINS, J. R. 1995. Regulation of the cyclin E gene by
887 transcription factor E2F1. *Proceedings of the National Academy of Sciences,* 92**,** 12146-
888 12150.
889 PAGANO, M., PEPPERKOK, R., VERDE, F., ANSORGE, W. & DRAETTA, G. 1992. Cyclin
890 A is required at two points in the human cell cycle. *The EMBO journal,* 11**,** 961-971.
891 PINHEIRO, D. & BELLAÏCHE, Y. 2018. Mechanical force-driven adherens junction
892 remodeling and epithelial dynamics. *Developmental cell,* 47**,** 3-19.
893 PIRRAGLIA, C., WALTERS, J. & MYAT, M. M. 2010. Pak1 control of E-cadherin endocytosis
894 regulates salivary gland lumen size and shape. *Development,* 137**,** 4177-4189.
895 PRADHAN, R., KUMAR, S. & MATHEW, R. 2023. Lateral adherens junctions mediate a
896 supracellular actomyosin cortex in drosophila trachea. *iScience,* 26.
897 PUCCI, B., KASTEN, M. & GIORDANO, A. 2000. Cell cycle and apoptosis. *Neoplasia,* 2**,** 291-
898 299.
899 RÖPER, K. 2012. Anisotropy of Crumbs and aPKC drives myosin cable assembly during tube
900 formation. *Developmental cell,* 23**,** 939-953.
901 ROYOU, A., FIELD, C., SISSON, J. C., SULLIVAN, W. & KARESS, R. 2004. Reassessing the
902 role and dynamics of nonmuscle myosin II during furrow formation in early Drosophila
903 embryos. *Molecular biology of the cell,* 15**,** 838-850.
904 RYOO, H. D., GORENC, T. & STELLER, H. 2004. Apoptotic cells can induce compensatory
905 cell proliferation through the JNK and the Wingless signaling pathways. *Developmental*
906 *cell,* 7**,** 491-501.
907 SANCHEZ-CORRALES, Y. E., BLANCHARD, G. B. & RÖPER, K. 2018. Radially patterned
908 cell behaviours during tube budding from an epithelium. *Elife,* 7**,** e35717.
909 SANCHEZ-CORRALES, Y. E., BLANCHARD, G. B. & RÖPER, K. 2021. Correct
910 regionalization of a tissue primordium is essential for coordinated morphogenesis. *Elife,*
911 10.
912 SARKISSIAN, T., TIMMONS, A., ARYA, R., ABDELWAHID, E. & WHITE, K. 2014.
913 Detecting apoptosis in Drosophila tissues and cells. *Methods,* 68**,** 89-96.
914 SIDOR, C. & RÖPER, K. 2016. Genetic control of salivary gland tubulogenesis in Drosophila.
915 *Organogenetic Gene Networks.* Springer.
916 SIDOR, C., STEVENS, T. J., JIN, L., BOULANGER, J. & RÖPER, K. 2020. Rho-kinase planar
917 polarization at tissue boundaries depends on phospho-regulation of membrane residence
918 time. *Developmental cell,* 52**,** 364-378. e7.
919 SIGRIST, S. J. & LEHNER, C. F. 1997. Drosophila fizzy-related down-regulates mitotic cyclins
920 and is required for cell proliferation arrest and entry into endocycles. *Cell,* 90**,** 671-681.
921 SLATTUM, G., MCGEE, K. M. & ROSENBLATT, J. 2009. P115 RhoGEF and microtubules
922 decide the direction apoptotic cells extrude from an epithelium. *Journal of Cell Biology,*
923 186**,** 693-702.
924 SMITH, A. V. & ORR-WEAVER, T. L. 1991. The regulation of the cell cycle during Drosophila
925 embryogenesis: the transition to polyteny. *Development,* 112**,** 997-1008.
926 SPINA, E. & COWIN, P. Embryonic mammary gland development. Seminars in Cell &
927 Developmental Biology, 2021. Elsevier, 83-92.
928 TOYAMA, Y., PERALTA, X. G., WELLS, A. R., KIEHART, D. P. & EDWARDS, G. S. 2008.
929 Apoptotic force and tissue dynamics during Drosophila embryogenesis. *Science,* 321**,**
930 1683-1686.

931 VISHWAKARMA, V., LE, T. P. & CHUNG, S. 2022. Multifunctional role of GPCR signaling
932 in epithelial tube formation. *Development,* 149**,** dev200519.
933 WEIGEL, D., SEIFERT, E., REUTER, D. & JÄCKLE, H. 1990. Regulatory elements
934 controlling expression of the Drosophila homeotic gene fork head. *The EMBO Journal,* 9**,**
935 1199-1207.
936 WESTERMANN, S. & WEBER, K. 2003. Post-translational modifications regulate microtubule
937 function. *Nature reviews Molecular cell biology,* 4**,** 938-948.
938 WILDE, J. J., PETERSEN, J. R. & NISWANDER, L. 2014. Genetic, epigenetic, and
939 environmental contributions to neural tube closure. *Annual review of genetics,* 48**,** 583-
940 611.
941 XU, N., BAGUMIAN, G., GALIANO, M. & MYAT, M. M. 2011. Rho GTPase controls
942 Drosophila salivary gland lumen size through regulation of the actin cytoskeleton and
943 Moesin. *Development,* 138**,** 5415-5427.
944 YAM, C., FUNG, T. & POON, R. 2002. Cyclin A in cell cycle control and cancer. *Cellular and*
945 *Molecular Life Sciences CMLS,* 59**,** 1317-1326.
946 YAMAGUCHI, Y., SHINOTSUKA, N., NONOMURA, K., TAKEMOTO, K., KUIDA, K.,
947 YOSIDA, H. & MIURA, M. 2011. Live imaging of apoptosis in a novel transgenic
948 mouse highlights its role in neural tube closure. *Journal of Cell Biology,* 195**,** 1047-1060.
949 ZAMZAMI, N. & KROEMER, G. 1999. Condensed matter in cell death. *Nature,* 401**,** 127-128.
950 ZIELKE, N., KIM, K. J., TRAN, V., SHIBUTANI, S. T., BRAVO, M.-J., NAGARAJAN, S.,
951 VAN STRAATEN, M., WOODS, B., VON DASSOW, G. & ROTTIG, C. 2011. Control
952 of Drosophila endocycles by E2F and CRL4CDT2. *Nature,* 480**,** 123-127.
953 ZIELKE, N., KORZELIUS, J., VAN STRAATEN, M., BENDER, K., SCHUHKNECHT, G. F.,
954 DUTTA, D., XIANG, J. & EDGAR, B. A. 2014. Fly-FUCCI: A versatile tool for
955 studying cell proliferation in complex tissues. *Cell reports,* 7**,** 588-598.

956

Sup. Fig. S1

A

***hkb-RA* transcript (1567bp)**

ORF in blue

ZnF domains highlighted (ZnF1, ZnF2, ZnF3)

gRNAs in bold and underlined (gRNA No.3 near the beginning of the ORF; gRNA No.1 in the 2nd ZnF domain)

GCTCAGTTCGAGTCGAGATCTCGCAGCACACACACAGCTCCGCACAACCAAATCAAGTCCAAAATCATAATCACA
AGTGTTCCATCCAAGTGATTTAGTGTCGCGAGAGAGCAATTTAGACCTTCCATTAAAACTACTGCAAAATGTCGA
CGATTAACCTGCATCC**CCCGCAAACCTACTCGCGACTTT**TCCGACCCTGGGATACTCAGCGCCAGGCGGCGAC
CTCGGCGGCACCCAGGACAGTGAAGCAGGAGCCGGAGGCGATTACCATCAAGACGGAGCTGGCCAGCAGCAG
TTTCGGCCACGACTGCGACGGAGACTTCTCCTCCGCATCCTCCTCTGCGTCAAGCAGCAGCAACAGCAGCAAGT
CCTGCTACGAGGAGGCCCTGAACCACAGCAGCTACACCCGCACTTCCACCCCGCTGCTGGACGCCGCCCCGC
ACCCCGTCTTTTCACACCCGCAGTCGTCGCCGTTGGACACGCACGCCGCCGCCACCGCATCCTTGGCTCCGCC
AAACCAGCACGCTCCATTCCTGTCGGCCGCCAGCGATCTCTACTACGCTGCCGCCGCCGCAGCAGCCGCTGCT
GCCTCCACGCCCACTGCCGTCCCGGGCTTCGGCATGGACCCGTTCACTATGGGCCTGATGGAGCAAGAGTACG
CCCGCGTGATGGCCGAGGACGCACAGTTAAAGGCGCTCAACAGCCGCAAGCAGCGGCCGAAGAAGTTCAAGT
GCCCCAACTGCGACGTGGCCTTCTCCAACAACGGCCAGCTGAAGGGCCACATCCGCATCCACACCGGCGAACG
CCCATTTAAGTGCGACGTGAACACATGCGGCAAGACCTTCA**CCCGCAATGAGGAACTGACGCGT**CACAAGCGA
ATCCACACCGGACTGCGGCCGTATCCTTGCAGTGCCTGCGGAAAGAAGTTTGGCCGACGCGACCACTTAAAGA
AGCACATGAAGACGCACATGCCGCAGGAGCGCCAGCTGGGCCCGTCCATCTTCGTGCCCATGTACTCATACCT
TTATGGCTACTGAGAGGGAAATCCTGGCGAGCTTTCCCCTTGCCACGCGACCCTGCATTCCAGCGATCTGTAAA
GCGCTTGCACGCTTTAAACAAGCATTACCGAACCGAATCCAACGAAACGAAACTTAACGCCAGCAAAAACTGCCT
AGCCAATCGTGGACAGAACTACCTCAGCCGTACCTGGCGCAATGTGGCGCACTCACCAAACCCAATCTTTGGAC
CTCGACGATATATGCAAATATTGAGATATTTATTTTTTAACGCGTATTTACACTTCCAGCTACGTGACTGGTTATGA
TATTCGGCACATGTGTAAATAATCCCTAAGTGATCCTTCCTCATATGCTAAGCGATTAAGAAATTTAAGAGATGCC
CGGATTTACGTCTAAGTTATACTAAAGCTGATACTTTAACAGTTTTATAAGCTGATCGTGGTTACCAGATACATAC
GATTTATACACAAAATTATACGATCATGGTTATATCTGAGAGTTGAATTATACGATTTATGTTTACAACACAAAATA
CACAAGAAAAACCG

B

***hkb*^{351} and *hkb*^{391} (gRNA No.3 sequence underlined in the WT sequence)**

WT ATGTCGACGATTAACCTGCATCCCCCGCAAACC TACTCGCGACTTTTCCGACCCTGGGATA
hkb^{351} ATGTCGACGATTAACCTGCATCCCCCGCAAACC T--CTCGCGACTTTTCCGACCCTGGGATA
hkb^{391} ATGTCGACGATTAA----------TCCCTGGGATACTCGCGACTTTTCCGACCCTGGGATA

***hkb*^{121} and *hkb*^{131} (gRNA No.1 sequence underlined in the WT sequence)**

WT ATGCGGCAAG ACCTTCACCCGCAATGAGGAACTGACGCGTCACAAGCGAATC
hkb^{121} ATGCGGCAAG ACCTTCACCCGCA------AGGAACTGACGCGTCACAAGCGAATC
hkb^{131} ATGCGGCAAGGTCT----------GGAACTGACGCGTCACAAGCGAATC

C

WT Hkb protein sequence (297aa; 3 ZnF domains)

MSTINLHPPQTYSRLFRPWDTQRQAATSAAPRTVKQEPEAITIKTELASSSFGHDCDGDFSSASSSASSSSNSSKSCY
EEALNHSSYTRTSTPLLDAAPHPVFSHPQSSPLDTHAAATASLAPPNQHAPFLSAASDLYYAAAAAAAAAASTPTAVP
GFGMDPFTMGLMEQEYARVMAEDAQLKALNSRKQRPKK**FKCPNCDVAFSNNGQLKGHIRIH**TGERP**FKCDVNTCG**
KTFTRNEELTRHKRIHTGLRP**YPCSACGKKFGRRDHLKKHMKTH**MPQERQLGPSIFVPMYSYLYGY

Mutant protein sequence in *hkb*^{121} (296 aa; substitution of N237 & E238 to K237 in the 2nd ZnF domain)

MSTINLHPPQTYSRLFRPWDTQRQAATSAAPRTVKQEPEAITIKTELASSSFGHDCDGDFSSASSSASSSSNSSKSCY
EEALNHSSYTRTSTPLLDAAPHPVFSHPQSSPLDTHAAATASLAPPNQHAPFLSAASDLYYAAAAAAAAAASTPTAVP
GFGMDPFTMGLMEQEYARVMAEDAQLKALNSRKQRPKK**FKCPNCDVAFSNNGQLKGHIRIH**TGERP**FKCDVNTCG**
KTFTRKELTRHKRIHTGLRP**YPCSACGKKFGRRDHLKKHMKTH**MPQERQLGPSIFVPMYSYLYGY

Truncated protein sequence in *hkb*^{131} (235 aa; 1 ZnF domain)

MSTINLHPPQTYSRLFRPWDTQRQAATSAAPRTVKQEPEAITIKTELASSSFGHDCDGDFSSASSSASSSSNSSKSCY
EEALNHSSYTRTSTPLLDAAPHPVFSHPQSSPLDTHAAATASLAPPNQHAPFLSAASDLYYAAAAAAAAAASTPTAVP
GFGMDPFTMGLMEQEYARVMAEDAQLKALNSRKQRPKK**FKCPNCDVAFSNNGQLKGHIRIH**TGERPFKCDVNTCG
KVWN

Truncated protein sequence in *hkb*^{351} (33 aa; no ZnF domains)

MSTINLHPPQTSRDFSDPGILSARRRPRRHPGQ

Mutant protein sequence in *hkb*^{391} (219 aa; No ZnF domains; only the first 5 aa is the same as WT (underlined))

<u>MSTIN</u>PWDTATFPTLGYSAPGGDLGGTQDSEAGAGGDYHQDGAGQQQFRPRLRRRLLLRILLCVKQQQQQQVLLR
GGPEPQQLHPHFHPAAGRRPAPRLFTPAVVAVGHARRRHRILGSAKPARSIPVGRQRSLLRCRRRSSRCCLHAHCR
PGLRHGPVHYGPDGARVRPRDGRGRTVKGAQQPQAAAEEVQVPQLRRGLLQQRPAEGPHPHPHRRTPI

Supplementary Fig. S1. Indels of CRISPR/Cas9 *hkb* alleles and predicted protein sequences for each allele. (A) The nucleotide sequence of the *hkb-RA* transcript. The open reading frame (ORF) is marked in blue. Three ZnF domains are highlighted in green (ZnF1), yellow (ZnF2) and magenta (ZnF3), respectively. Two gRNA sequences used to create *hkb* alleles are indicated in bold and underlined. (B) CRISPR/Cas9-introduced indels in *hkb* mutants. Nucleotides deleted and inserted in each mutant are indicated in dashed lines and in red, respectively. (C) Sequences of the WT Hkb protein and predicted proteins in each *hkb* mutant.

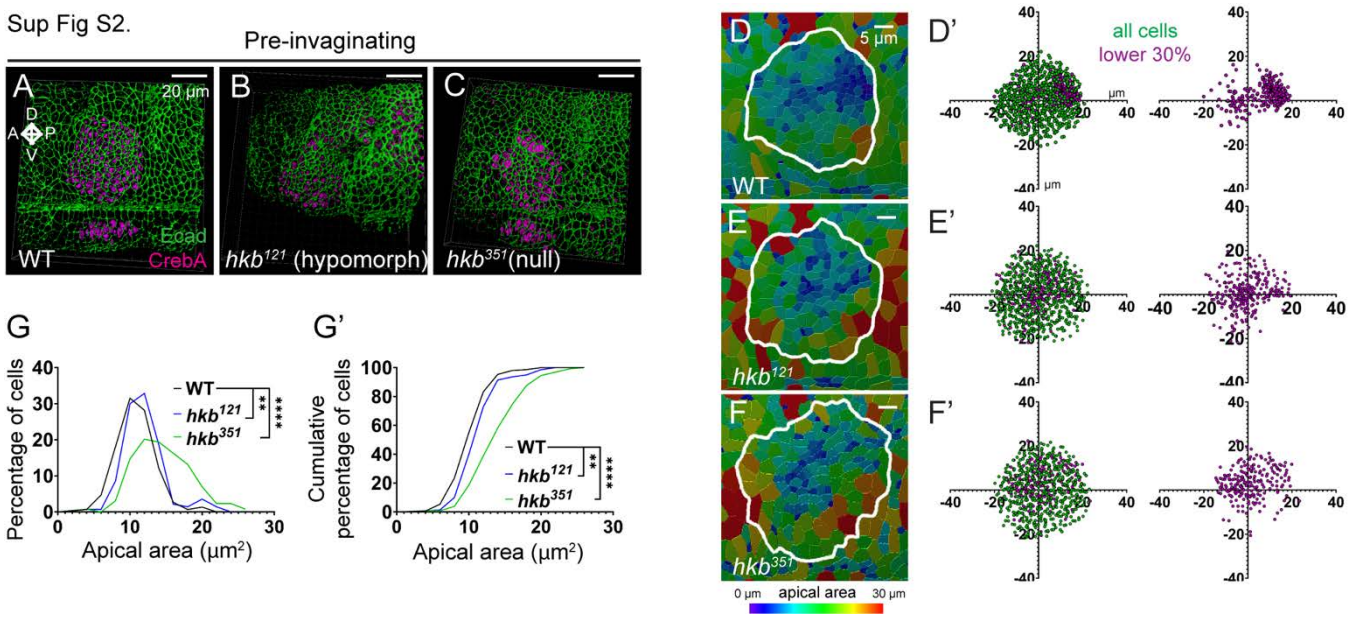

Supplementary Fig. S2. Quantification of apical areas in the pre-invaginating SG of WT and *hkb* mutant embryos. (A-C) Three-dimensional reconstruction of confocal images of pre-invaginating SGs immunolabeled with Ecad and CrebA. (D-F) Heat maps of apical area distribution in pre-invaginating SGs. (D'-F') Scatter plots showing the relative position of total SG cells (green) and cells with small apical areas (magenta). X and Y axes represent the distance along the A/P and D/V axes, respectively, from the center of the placode. Cells in the bottom 30% of the apical area (magenta) and all cells (green) are plotted. (G, G') Quantification of apical area distribution in SG cells before invagination. Mann-Whitney U test (percentage of cells) and Kolmogorov-Smirnov test (cumulative percentage of cells). N=7 (WT, 932 cells; *hkb*^{121}, 727 cells; *hkb*^{351}, 864 cells). **, $p<0.05$; ****, $p<0.0005$.

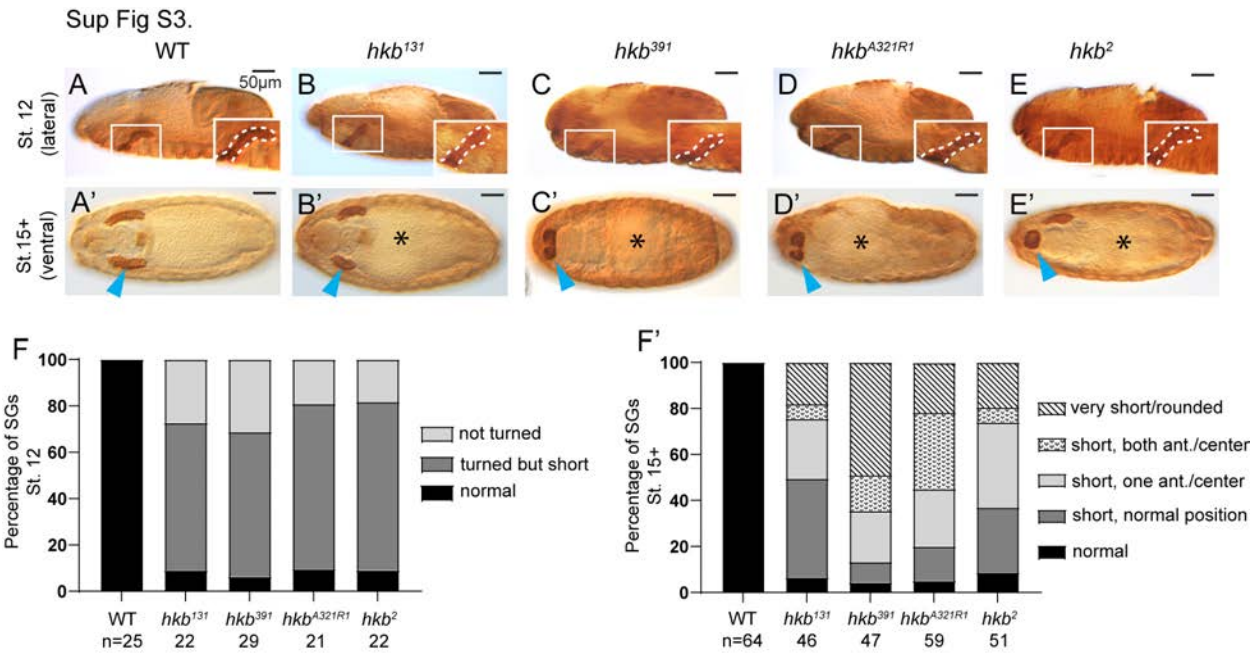

Supplementary Fig. S3. SG phenotypes in different *hkb* alleles. (A-E') Stage 12 (A-E; lateral) and stage 15+ (A'-E'; ventral) of embryos immunostained for CrebA. The insets show a magnified view of the region in the white rectangles, with the SG outlined by white dashed lines. Cyan arrowheads, SGs in stage 15+ embryos. Asterisks, defective gut morphology. (F, F') Quantification of the SG phenotypic distribution at stage 12 (F) and stage 15 (F'). The number of embryos used is indicated below each genotype. Statistical significance was calculated using two-way ANOVA.

Sup Fig S4.

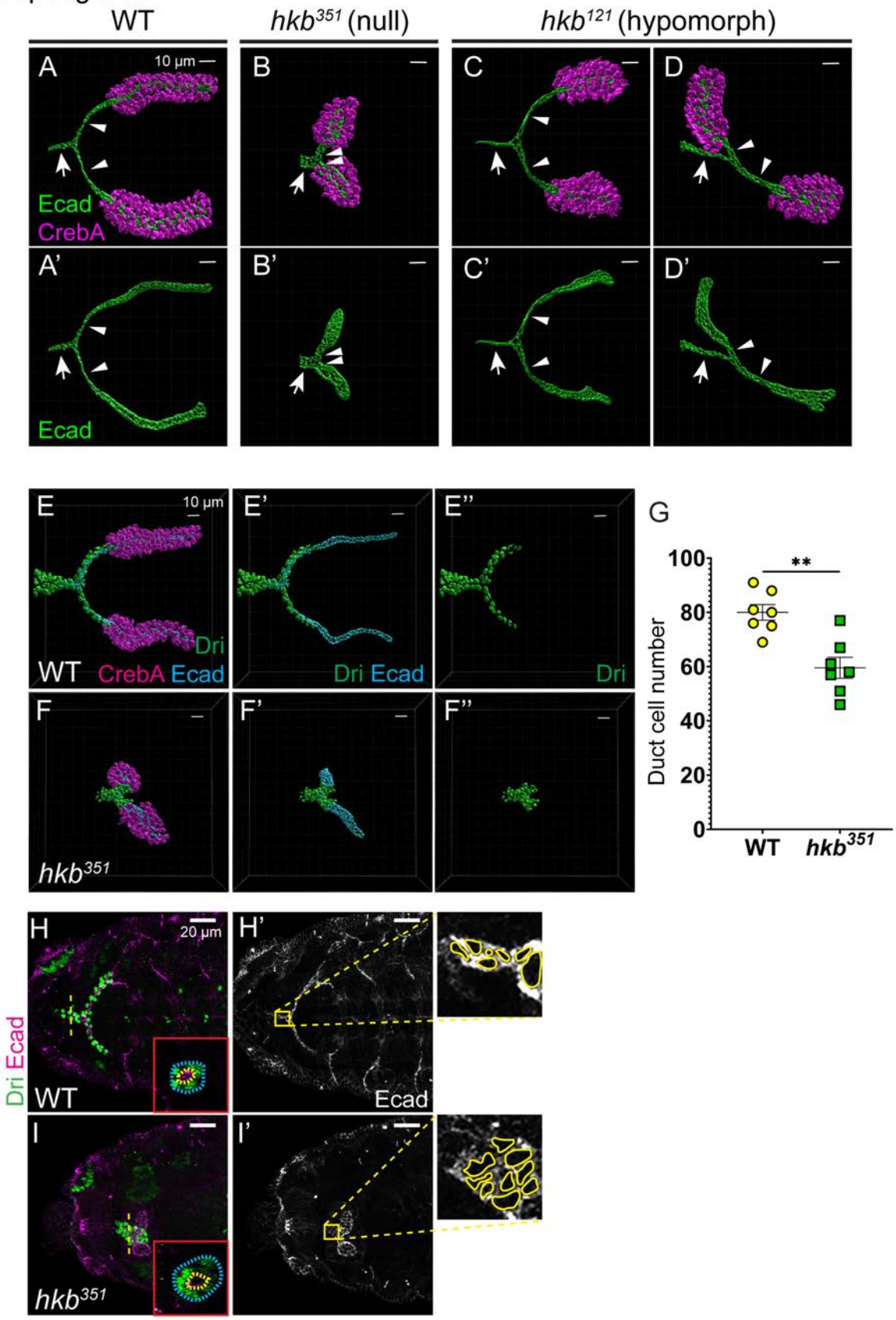
WT
hkb351 (null)
hkb121 (hypomorph)
A
10 µm
B
C
D
Ecad
CrebA
A'
B'
C'
D'
Ecad
E
10 µm
E'
E''
Dri
WT
CrebA
Ecad
Dri
Ecad
Dri
F
F'
F''
hkb351
G
**
Duct cell number
100
80
60
40
20
0
WT
hkb351
H
20 µm
H'
Dri
Ecad
WT
Ecad
I
I'
hkb351

Supplementary Fig. S4. *hkb* mutants show short salivary duct phenotypes with reduced cell numbers and cell intercalation defects. (A-D') 3D reconstruction of the confocal images of stage 15+ SGs immunolabeled with Ecad (green) and CrebA (magenta). Arrows, common duct. Arrowheads, individual duct. (E-F'') 3D reconstruction of the confocal images of stage 15+ SGs immunolabeled with Dri (green), CrebA (magenta), and Ecad (cyan). (G) Quantification of the duct cell numbers. N=7. Statistical significance was calculated using Student's t-test. (H-I') Confocal images of SGs immunolabeled with Ecad (magenta) and Dri (green). Z-sections along the yellow dashed lines in H and I are shown as insets. Yellow boxed regions in H' and I' are shown at higher magnification, with the boundary of each salivary duct cell marked with yellow lines.

Sup Fig S5.

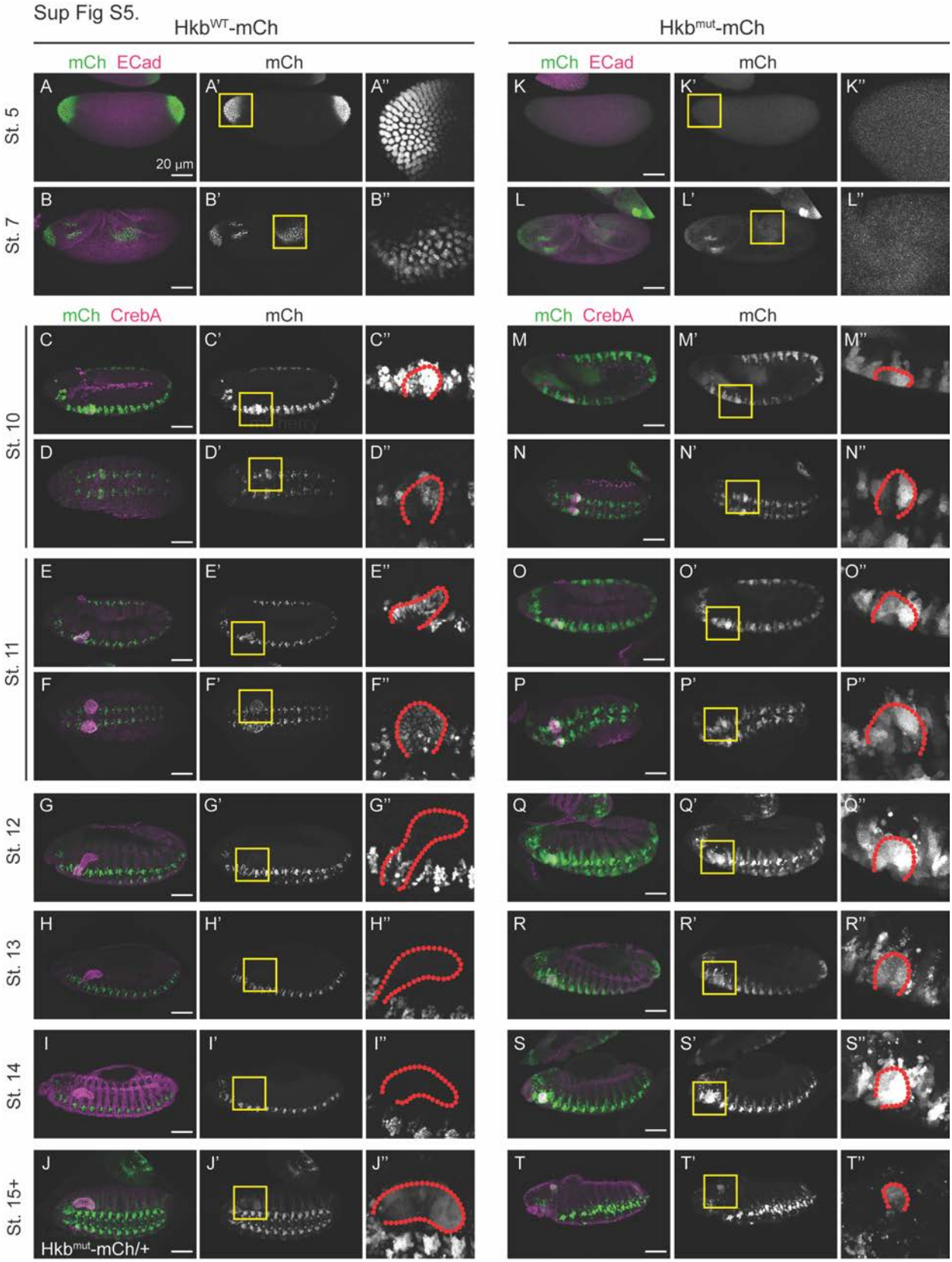
Hkb^{WT}-mCh
Hkb^{mut}-mCh
mCh ECad
mCh
mCh CrebA
St. 5
St. 7
St. 10
St. 11
St. 12
St. 13
St. 14
St. 15+
20 µm
Hkb^{mut}-mCh/+

Supplementary Fig. S5. Hkb^{wt}-mCh and Hkb^{mut}-mCh signals during embryonic development. (A-T'') Hkb^{wt}-mCh (A-I'') and Hkb^{mut}-mCh (J-T'') expression patterns in embryos at different stages. Yellow boxed regions in A'-T' are shown in higher magnification in A''-T''. SGs are outlined by red dotted lines in M''-T''. (A-A'') At stage 5, Hkb^{wt}-mCh signals localize to the nuclei of the cells at the anterior and posterior poles of the embryo. (B-B'') At stage 7, Hkb^{wt}-mCh signals are seen in the nuclei of the anterior region and in the posterior midgut of the embryo. (C-D'') At stage 10, strong nuclear Hkb^{wt}-mCh signals are seen along the CNS and in the posterior region of the SG of the embryo. mCherry signals localize to the nuclei of the cells. (C-C'') Lateral view. (D-D'') Dorsal view. (E-F'') At stage 11, strong nuclear Hkb^{wt}-mCh signals are seen in all SG cells. (G-G'') At stage 12, Hkb^{wt}-mCh signals are significantly reduced in SG nuclei, while the mCh signals are consistently high in cells of the CNS. (H-H'') At stage 13, very low levels of Hkb^{wt}-mCh signals are seen in the SG nuclei. (I-I'') At stage 14, the Hkb^{wt}-mCh signals of the SG nuclei are reduced to almost undetectable levels. (J-T'') Hkb^{mut}-Ch signals are seen throughout the cell. (J-J'') mCh signals in Hkb^{mut}-mCh/+ heterozygous embryo at stage 16. mCh signals persist in the SG. (M-T'') mCh signals in Hkb^{mut}-mCh homozygous embryos. mCh signals persist in the SG throughout embryogenesis and are seen throughout the cell.

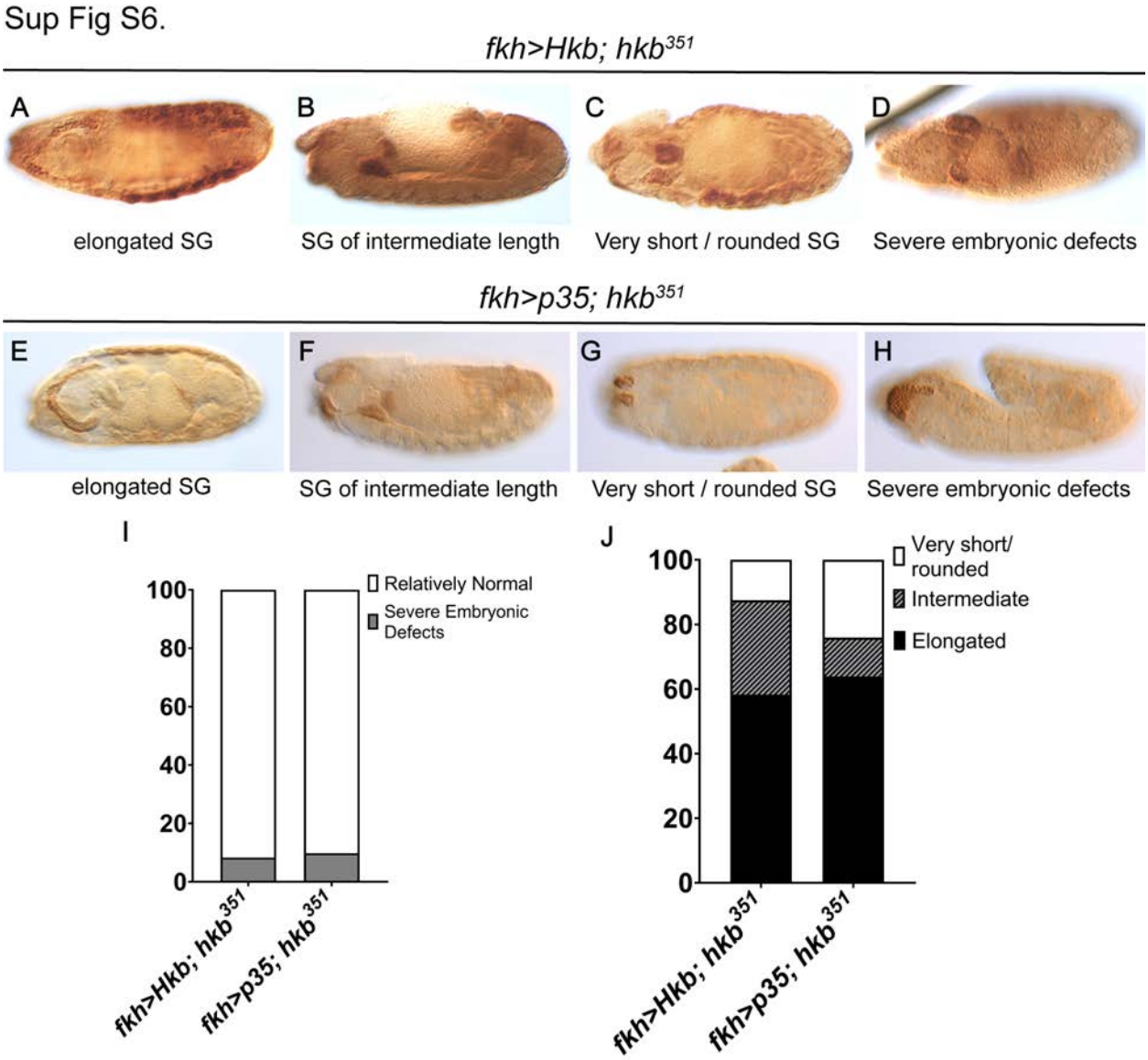

Supplementary Fig. S6. Overexpression of Hkb or p35 partially rescues the SG phenotypes of *hkb* mutants. (A-H) Embryos stained for CrebA. Overexpression of Hkb (A-D) or p35 (E-H) in the SG using the *fkh-Gal4* driver in the *hkb* mutant background results in a range of the phenotypes, including fully elongated SGs as in WT (A, E), SGs of intermediate length (B, F), SGs with a very short/rounded phenotype as in *hkb* null mutants (C, G). Some embryos also show severe morphological defects (D, H). (I, J) Quantification of the SG morphology. Embryos with relatively normal morphology as shown in A-C and E-G were used for quantification. N=24 (*fkh>Hkb*; hkb^{351}) and 92 (*fkh>p35*; hkb^{351}) embryos. Statistical significance was calculated using two-way ANOVA.

Sup Fig S7.

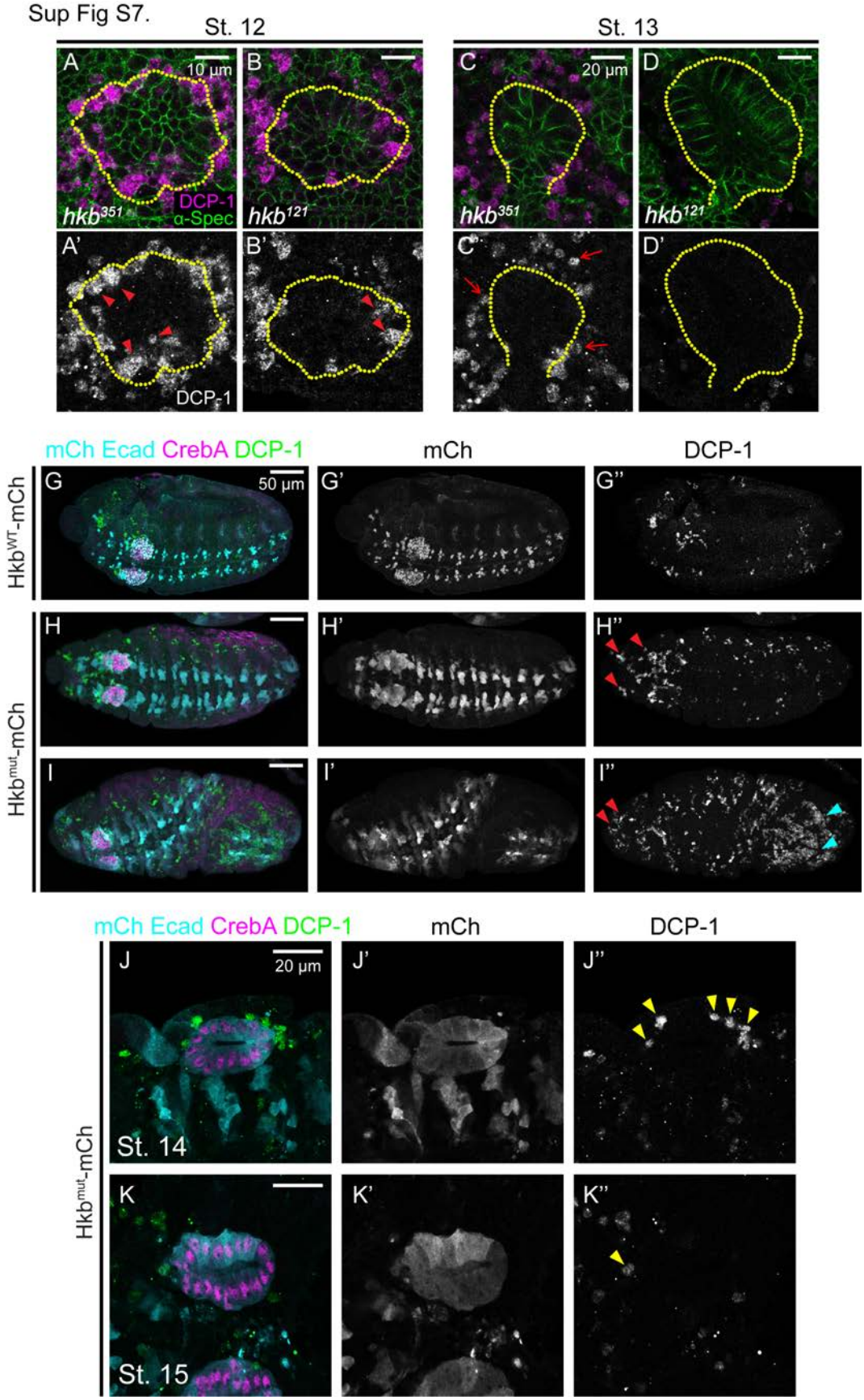
St. 12
St. 13
A
10 µm
B
C
20 µm
D
DCP-1
α-Spec
hkb351
hkb121
hkb351
hkb121
A'
B'
C'
D'
DCP-1
mCh Ecad CrebA DCP-1
mCh
DCP-1
HkbWT-mCh
G
50 µm
G'
G''
Hkbmut-mCh
H
H'
H''
I
I'
I''
mCh Ecad CrebA DCP-1
mCh
DCP-1
Hkbmut-mCh
J
20 µm
J'
J''
St. 14
K
K'
K''
St. 15

Supplementary Fig. S7. DCP-1 signals in late-stage SGs and in the other region of *hkb* mutant embryos. (A-D') Confocal images of SGs in stage 12 and 13 *hkb* mutant embryos immunostained for α-Spec (green) and DCP-1 (magenta). Yellow dotted lines, SG boundary. Arrowheads in A' and B', DCP-1 signals in the cells within the SG placode. Arrows in C, DCP-1-positive cells near the SG placode in the *hkb* null mutant embryo. (G-I'') Confocal images of stage 11 embryos immunostained for Ecad and mCh (cyan), CrebA (magenta), and DCP-1 (green). Hkb^{mut}-mCh embryos show increased DCP-1 signals in other regions of the embryo compared to Hkb^{WT}-mCh embryos, with a greater increase in the head region (red arrowheads) and posterior region (cyan arrowheads in I''). (J-K'') Confocal images of SGs in stage 14 and 15 Hkb^{mut}-mCh embryos stained for mCh and Ecad (cyan), CrebA (magenta), and DCP-1 (green). Arrows in J'', DCP-1-positive cells near the SG at stage 14.

Sup Fig S8.

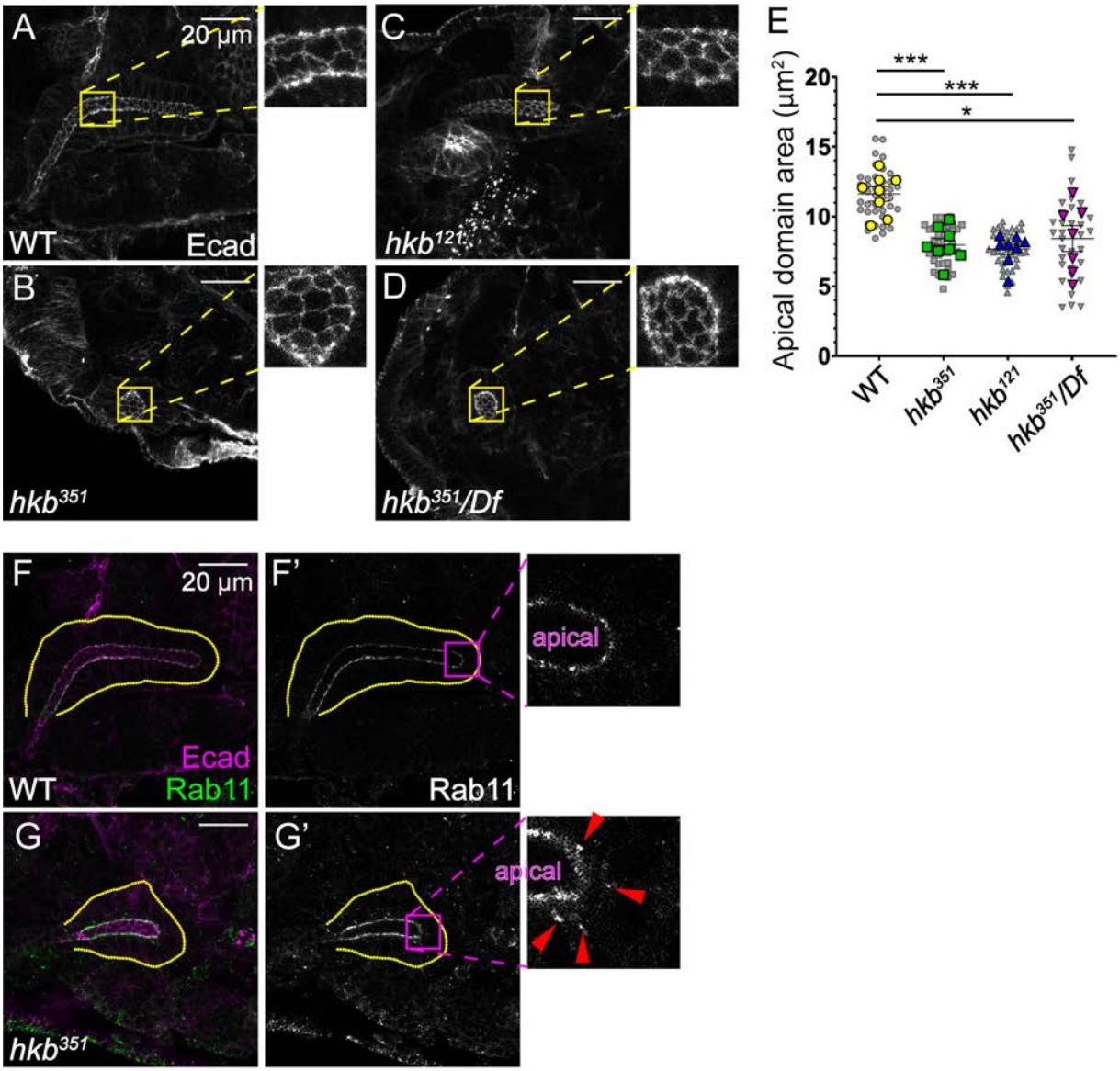

Supplementary Fig. S8. *hkb* mutant SGs have a smaller apical domain size with Rab11 mislocalized to the basolateral domain. (A-D) Confocal images of SGs in stage 15 embryos immunostained for Ecad. Apical domains in the yellow boxed regions are shown at higher magnification. (E) Quantification of the apical area of individual SG cells. (F, G) Confocal images of SGs in stage 15 embryos immunostained for Rab11. Magenta boxed regions are shown at higher magnification. Yellow dotted lines, basal boundary of the SG. Red arrowheads, small punctate Rab11 signals often observed in the basolateral region of SG cells in *hkb* mutants.

Sup Fig S9.

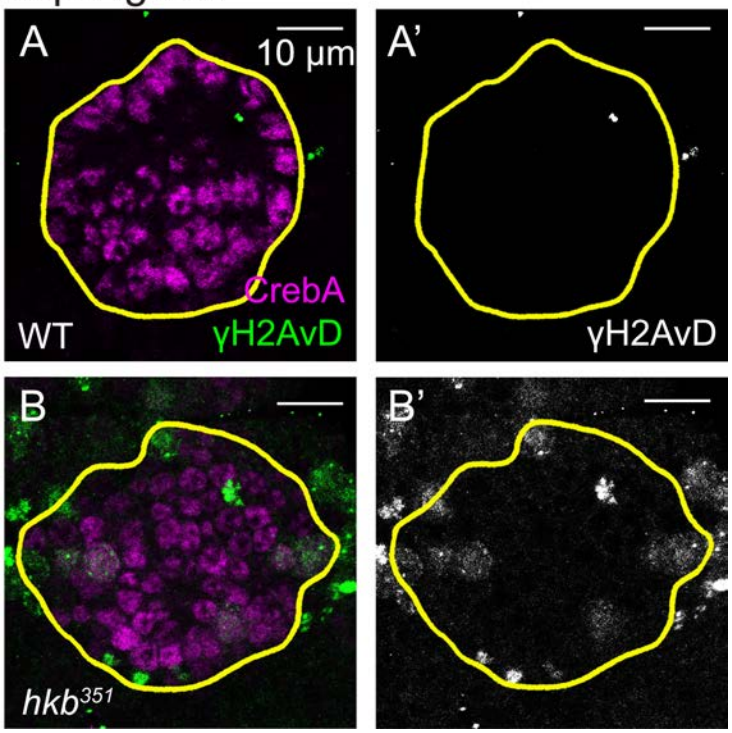

Supplementary Fig. S9. γ-H2Av signals in stage 11 *hkb* mutant SGs. (A-B') Confocal images of SGs in WT (A-A') and *hkb* mutant (B-B') embryos immunostained for CrebA (magenta) and γ-H2Av (green). *hkb* mutant SGs show an increase in γ-H2Av signals in the entire placode compared to WT. Yellow lines, SG boundary.

Sup Fig S10.

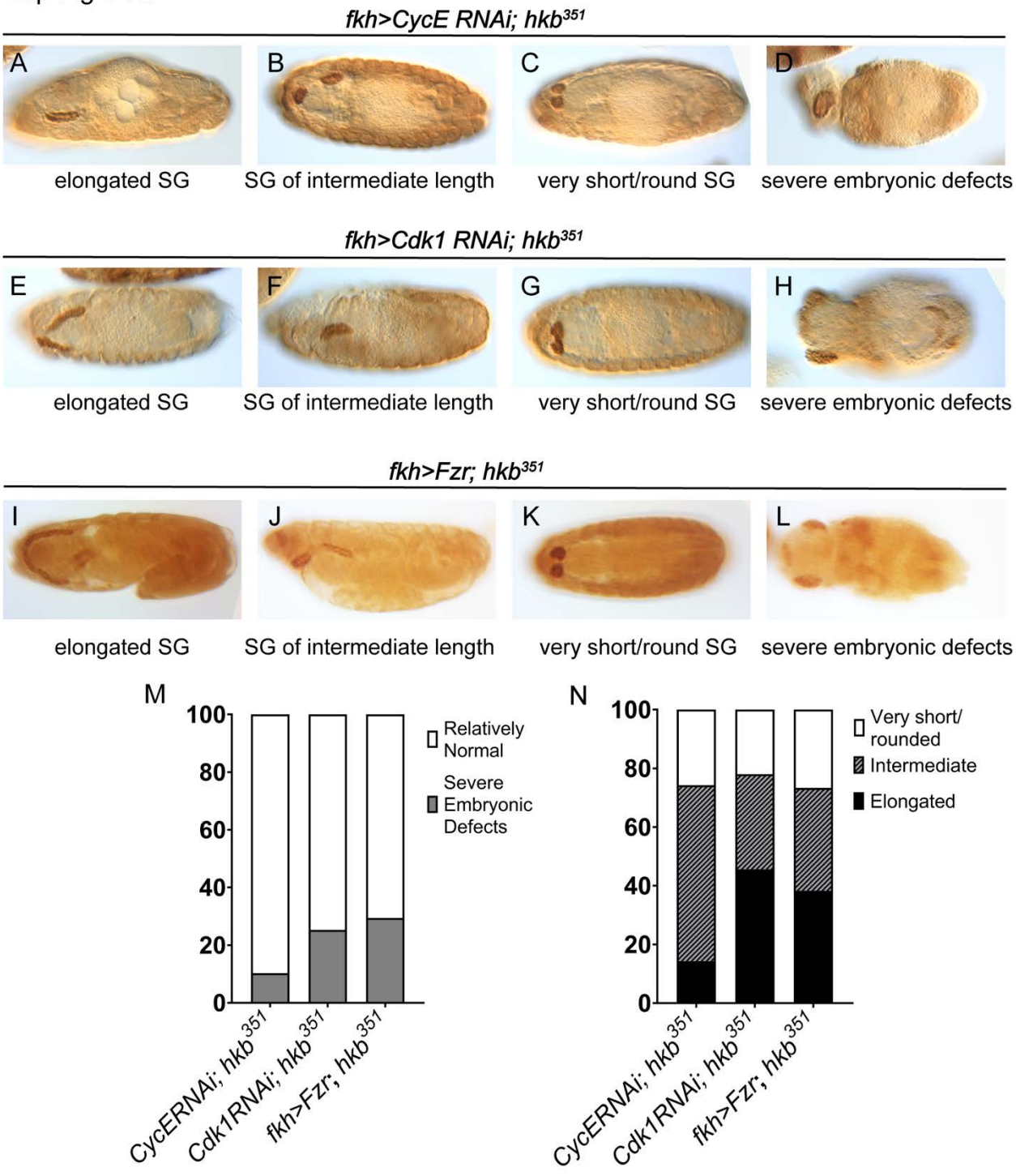
fkh>CycE RNAi; hkb351
A
B
C
D
elongated SG
SG of intermediate length
very short/round SG
severe embryonic defects
fkh>Cdk1 RNAi; hkb351
E
F
G
H
elongated SG
SG of intermediate length
very short/round SG
severe embryonic defects
fkh>Fzr; hkb351
I
J
K
L
elongated SG
SG of intermediate length
very short/round SG
severe embryonic defects
M
100
80
60
40
20
0
Relatively Normal
Severe Embryonic Defects
CycERNAi; hkb351
Cdk1RNAi; hkb351
fkh>Fzr; hkb351
N
100
80
60
40
20
0
Very short/ rounded
Intermediate
Elongated
CycERNAi; hkb351
Cdk1RNAi; hkb351
fkh>Fzr; hkb351

Supplementary Fig. S10. Knockdown of *Cdk1* or *CycE* partially rescues the SG phenotypes of *hkb* mutants. (A-H) Embryos stained for CrebA. Knockdown of *CycE* (A-D) or *Cdk1* (E-H), or overexpression of Fzr (I-L) in the SG using the *fkh-Gal4* driver in the *hkb* mutant background results in a range of the phenotypes, including fully elongated SGs as in WT (A, E, I), SGs of intermediate length (B, F, J), SGs with a very short/rounded phenotype as in *hkb* null mutants (C, G, K). Some embryos also show severe morphological defects (D, H, L). (M, N) Quantification of the SG morphology. Embryos with normal morphology as shown in A-C, E-G, and I-K were used for quantification. N=68 (*fkh>Cdk1RNAi*; hkb^{351}), 35 (*fkh>CycERNAi*; hkb^{351}), and 60 (*fkh>Fzr; hkb*) embryos. Statistical significance was calculated using two-way ANOVA.

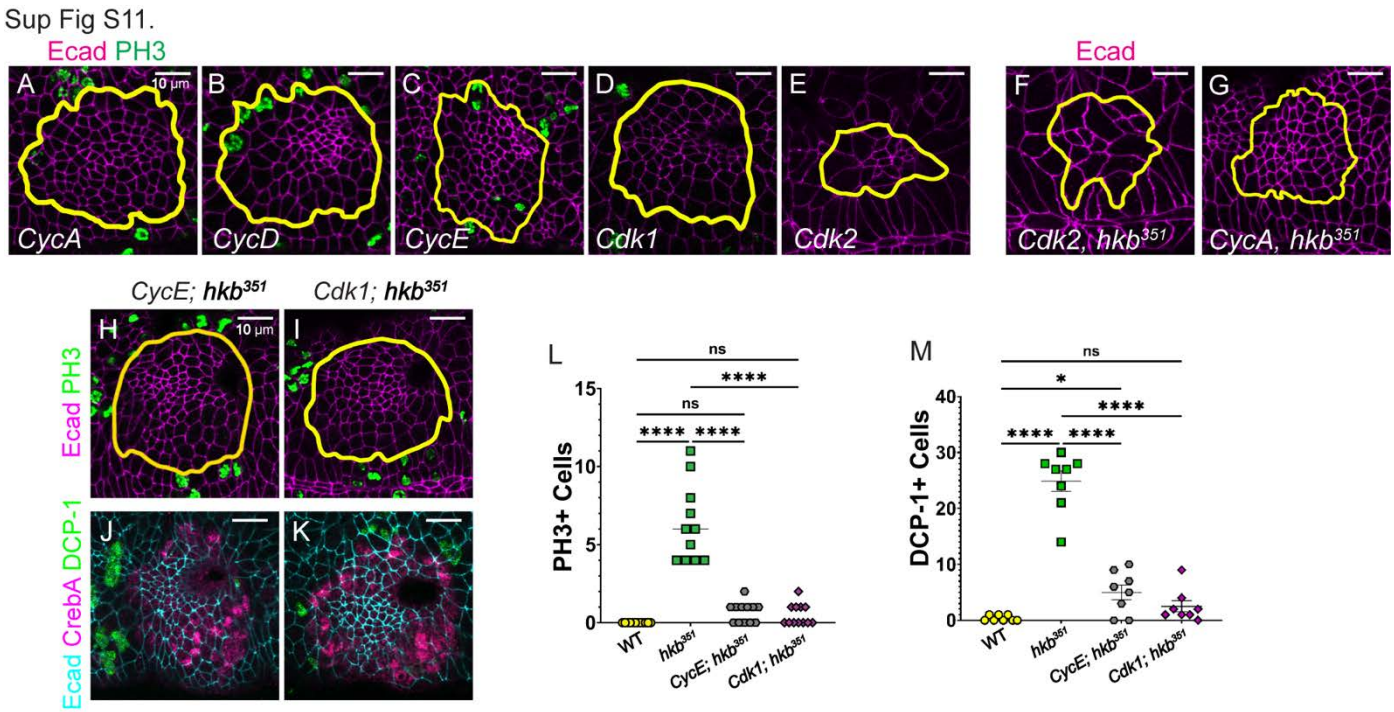

Supplementary Fig. S11. Embryos double mutant for *Cdk1* or *CycE* and *hkb* have a reduced number of cell divisions and cell deaths in the SG. (A-E) SGs in stage 11 embryos for single mutants for key cell cycle genes, immunostained for Ecad (magenta) and PH3 (green). Single mutants for *CycA*, *CycD*, *CycE*, and *Cdk1* have relatively normal SG morphology, with few SG cells expressing PH3 (green) in *CycD* and *CycE* mutants. *Cdk2* mutant embryos have severe morphological defects, including significantly fewer SG cells. (F, G) SGs in stage 11 embryos double mutant for *Cdk2* and *hkb* (F) and *CycA* and *hkb* (G). *Cdk2 hkb* double mutant embryos show severe morphological defects similar to *Cdk2* single mutant embryos, with significantly reduced SG cell numbers. *CycA hkb* double mutants show the same range of phenotypes as *hkb* mutants, including the centralized invagination phenotype. (H-K) SGs in stage 11 double mutant embryos of *CycE* and *hkb* (H, J) and *Cdk1* and *hkb* (I, K). (H, I) Embryos are immunostained for Ecad (magenta) and PH3 (green). (J, K) Embryos are immunostained for Ecad (cyan), CrebA (magenta), and DCP-1 (green). (L, M) Quantification of the number of PH3-positive (L) and DCP-1-positive SG cells. (M) SG cells at stage 11. N= 12 SGs (PH3 quantification) for all genotypes and 8 SGs (DCP-1 quantification) for all genotypes. Statistical significance was calculated using a one-way ANOVA test with multiple comparisons.

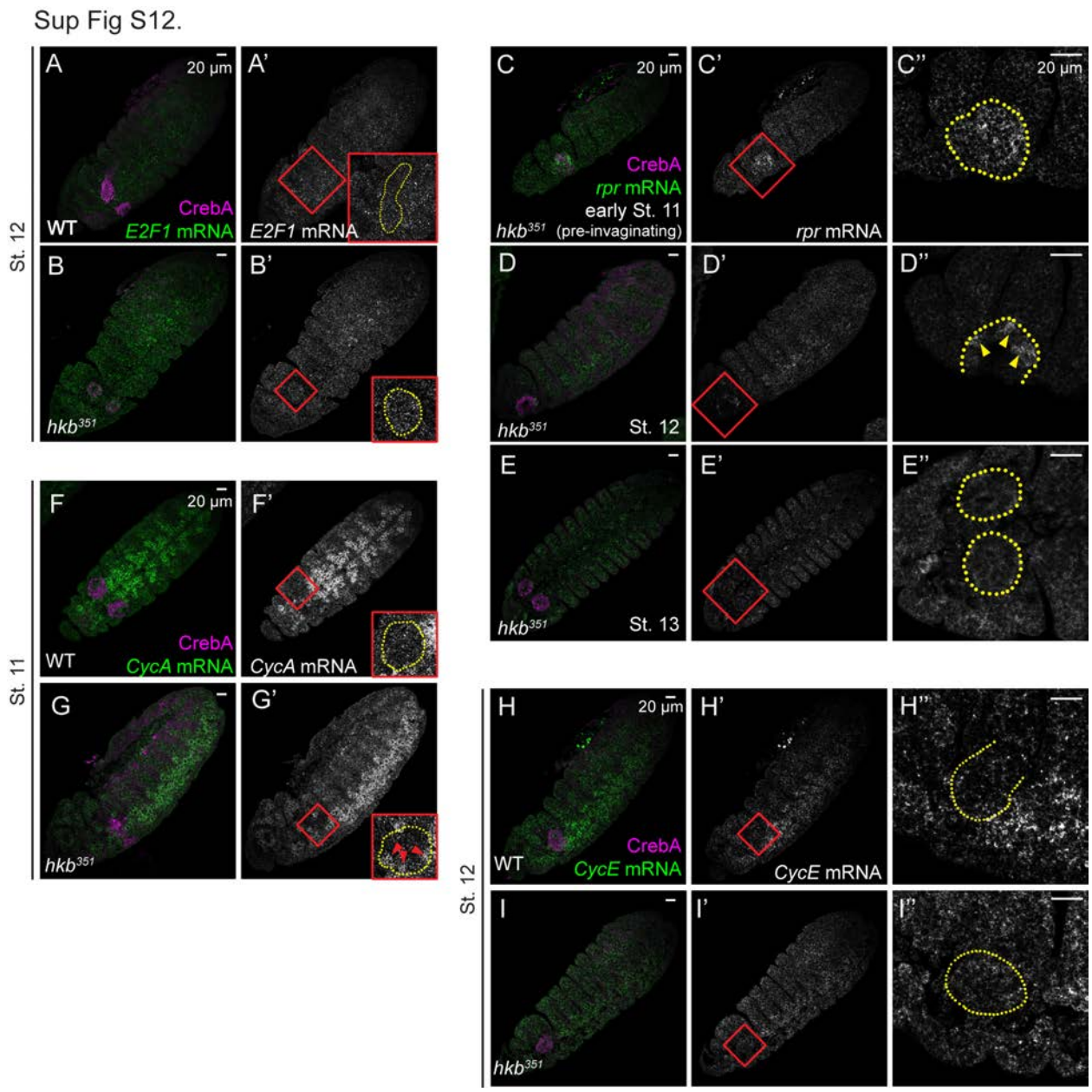

Supplementary Fig. S12. Expression levels of key cell cycle and cell death genes that are transcriptional targets of Hkb. (A-F') Confocal images of embryos from fluorescence *in situ* hybridization experiment showing the mRNA levels of *E2F1* at stage 12 (A-B'), *rpr* at stages 11-13 (C-E''), *CycA* at stage 11 (F-G'), and *CycE* at stage 12 of embryogenesis (H-I''). (A-B') In WT SGs, *E2F1* mRNA shows basal levels comparable to neighboring cells. In *hkb* mutant SGs, *E2F1* transcript levels are slightly higher than in neighboring cells. (C-E'') *rpr* mRNA expression is significantly upregulated in the pre-invaginating *hkb* mutant SG compared to neighboring cells. At stage 12, a few SG cells maintain high *rpr* levels (yellow arrowheads). At

stage 13, significant *rpr* transcript levels are very low in the SG. (F-G') In WT SGs, *CycA* shows placode-wide underexpression. In *hkb* mutants, *CycA* mRNA levels are significantly elevated in some SG cells (red arrowheads). (H-I'') In WT SGs, *CycE* shows placode-wide underexpression at stage 12. In *hkb* mutant SGs, *CycE* mRNA levels are slightly elevated and comparable to neighboring cells. Red boxes show the SG regions at higher magnification shown as insets in A', B', F', and G' and in C''-E'', H''-I''. Yellow dotted lines indicate the SG boundary.